Journal of Sound and Vibration 354 (2015) 65–90

Contents lists available at ScienceDirect

Journal of Sound and Vibration

journal homepage: www.elsevier.com/locate/jsvi

On the aeroacoustic and flow structures developed on a flat plate with a serrated sawtooth trailing edge

Tze Pei Chong *, Alexandros Vathylakis

College of Engineering, Design and Physical Sciences, Brunel University London, Uxbridge UB8 3PH, United Kingdom

ARTICLE INFO

Article history:
Received 1 October 2014
Received in revised form
10 May 2015
Accepted 14 May 2015
Handling Editor: P. Joseph
Available online 30 June 2015

ABSTRACT

Results of an experimental study on turbulent flow over a flat plate with a serrated sawtooth trailing edge are presented in this paper. After tripping the boundary layer to become turbulent, the broadband noise sources at the sawtooth serrated trailing edge is studied by several experimental techniques. Broadband noise reduction by the serrated sawtooth trailing edge can be realistically achieved in the flat plate configuration. The variations of wall pressure power spectral density and the spanwise coherence (which relates to the spanwise correlation length) in a sawtooth trailing edge play a minor role in the mechanisms underpinning the reduction of self noise radiation. Conditional-averaging technique was applied in the boundary layer data where a pair of pressure-driven oblique vortical structures near the sawtooth side edges is identified. In the current flat plate configuration, the interaction between the vortical structures and the local turbulent boundary layer results in a redistribution of the momentum transport and turbulent shear stress near the sawtooth side edges as well as the sawtooth tip, thus affecting the efficiency of self noise radiation.

1. Introduction

Self noise emitted from the trailing edge of an airfoil blade represents a major environmental and operational issue in aviation, wind turbine and home appliance industries. There has been much interest recently in developing flow control methods aimed at reducing trailing edge self noise. For example, active flow control of wall-normal suction method was implemented at wind turbine blade to reduce trailing edge noise [1]. Another active flow control method for the suppression of trailing edge self noise is achieved by the Dielectric Barrier Discharge plasma actuators [2]. In this case, the induced air jet by the actuators can disrupt the growth of the boundary layer instabilities, thus resulting in the suppression of instability tonal noise.

In terms of airfoil self noise reduction by passive flow control, one of the most commonly used methods is inspired by the owl's wing. The unique feature of trailing edge serration is known to be quite effective in reducing both aerodynamic drag [3,4] and self noise radiation [5–11]. The serration has been studied in several forms: M-shaped [3,4], wavy [5] and sawtooth [6–11]. This paper focuses specifically on the sawtooth shape. A comprehensive experimental study by Gruber et al. [9] on many sawtooth geometries has established that significant noise reduction can be achieved if two conditions are fulfilled. The first is when the serration length is of the same order as the turbulent boundary layer thickness near the trailing edge.

* Corresponding author.
E-mail address: t.p.chong@brunel.ac.uk (T.P. Chong).

http://dx.doi.org/10.1016/j.jsv.2015.05.019
0022-460X/

The second is when the serration angle is small, giving the appearance of a sharp sawtooth. These conditions generally agree well with the recommendation given by Howe [6].

In the case of a fully turbulent boundary layer, for example at high Reynolds numbers, or when tripping is applied, some of the turbulent energy in the boundary layer will be scattered into broadband noise at the trailing edge. The relationship between the far field acoustic pressure and the near field surface pressure near the trailing edge is made explicit in the classical work of Amiet [12] who derived a direct relationship between the power spectral density of the far field noise S_{pp} in terms of the spanwise correlation length l_y and the surface pressure spectrum S_{qq} near the trailing edge, and a radiation term $L(\omega)$, of the form $S_{pp}(\omega) \propto L(\omega) l_y(\omega) S_{qq}(\omega)$. This result predicts a reduction in the radiated broadband noise if the level of either l_y, S_{qq} and/or $L(\omega)$ is reduced. A sawtooth surface has the potential to modify one or more of the above three source terms, possibly leading to a reduction of the radiated noise.

The theoretical approach of Howe [6] assumes that as soon as obliqueness is introduced at the trailing edge, the coherences between the acoustic sources along the wetted edge will be reduced which ultimately result in a weaker noise radiation. The unsteady wall pressure spectrum in Howe's equations, however, is formulated by Chase's wall pressure model [13] for both the straight and serrated trailing edges. This implies that Howe disregards the hydrodynamic changes of the turbulent boundary layer over a serrated sawtooth trailing edge. The validity of this assumption has not been explicitly addressed.

In their investigation of the laminar instability tonal noise, Chong and Joseph [14] measured the boundary layer velocity power spectral density on the serrated sawtooth trailing edge at the pressure surface of a NACA0012 airfoil at 4.2° effective angle of attack. They observed that the boundary layer velocity spectrum actually exhibits increasingly turbulent characteristics towards the sawtooth tip. Moreau and Doolan [15] studied the near wake of a flat-plate with two kinds of serrated sawtooth trailing edges. They reported the modification of the wake characteristics in the serrated trailing edge and concluded that the upstream boundary layer must be modified by the serrated sawtooth trailing edge. A dissertation published by Pröbsting [16] provided some aerodynamic results on a nonflat plate type serrated trailing edge on a NACA0012 airfoil. By utilizing a tomographic PIV technique, a subset of coherent structures near the trailing edge was identified. Due to the blunt root of the serration, some longitudinal vortex shedding events have also been identified on the sawtooth surface, which apparently can produce tonal noise of a similar shedding frequency. Pröbsting [16] postulated that, through the vortex shedding event, the reduction in broadband noise by trailing edge serration could be related to the redistribution of energy within the turbulence spectrum.

Despite the recent publications by many authors on the subject, a consensus on the mechanism of broadband noise reduction by the serrated sawtooth trailing edge has not been reached. The main reason is that a more fundamental study on the boundary layer characteristics over a sawtooth surface remains scarce, especially from the experimental point of view. The expression from Amiet [12], which correlates the radiated acoustic pressure to the scattering of the hydrodynamic pressure waves near the trailing edge, provides an avenue for the investigation of the noise reduction mechanism by comparing the full wall pressure fields between a straight trailing edge and a serrated sawtooth trailing edge. However, it is very difficult to perform the above task when the serration is applied to an airfoil's trailing edge. This is because the physical size of the microphone will prohibit the wall pressure measurement at locations close to the side edges and tips of the sawtooth. In this work, a simple flat plate model was flush mounted to one side of the wind tunnel exit nozzle. The microphone can then be connected freely from the underside of the flat plate, which will allow wall pressure to be measured close to the trailing edges.

Self noise radiated by the above flat plate configuration for both the straight trailing edge and serrated sawtooth trailing edge was measured in an aeroacoustic facility. The noise results demonstrate that trailing edge broadband noise reduction can be realistically achieved by the serrated sawtooth trailing edge. This justifies the use of the flat plate model for the investigation of the noise reduction mechanism by serrated sawtooth trailing edge. The main parameters which are investigated in this paper include the unsteady wall pressure power spectral densities *(PSD)*, coherence functions and heat transfer characteristics across a full sawtooth surface. Boundary layer velocity measurements were performed to obtain the time-averaged velocity *PSD* and the Reynolds shear stresses. The boundary layer velocity signals were also conditionally-averaged to produce temporal variation of the momentum/turbulence properties across a sawtooth surface. An outlook section is provided to connect the observations in a flat plate to that of an airfoil, where both are subjected to serrated sawtooth trailing edges. It is hoped that the results presented in this paper can help to improve the understanding of the fundamental mechanism underpinning the reduction of self noise by a serrated sawtooth trailing edge, and also to provide an avenue for further development of other control techniques based on similar physical principles.

2. Experimental setup

2.1. Wind tunnels and test models

The aerodynamic measurements were conducted in an open jet wind tunnel which can achieve a maximum speed of about 35 m s^{-1}. Throughout the experiment, the freestream velocity was maintained at 30 m s^{-1}. The cross sectional area of the nozzle outlet is 50 mm × 150 mm. A flat plate extension of 150 mm × 295 mm was attached to one side of the nozzle lip, which is interchangeable with other flat plate models. Note that the background noise level produced by this open jet wind tunnel is excessive and cannot be used for any meaningful noise measurement.

Aeroacoustic measurements were instead conducted in a newly built anechoic chamber and open jet wind tunnel at Brunel University London [17]. The dimension of the anechoic chamber is 5 m × 4 m × 3.5 m. The open jet wind tunnel is driven by a centrifugal fan outside the chamber and the air flow inside the tunnel is acoustically treated by a 10 m long silencer. The cross sectional area of the nozzle exit is 100 mm × 300 mm. A flat plate extension of 300 mm × 295 mm was flush mounted to one side of the exit nozzle. The lengths of the flat plates for both aerodynamic and aeroacoustic experiments are exactly the same.

Note that this aeroacoustic facility only became available after all the aerodynamic measurements have been completed. In this paper, only results in Figs. 4 and 7a were obtained in this aeroacoustic facility; the rest were obtained in the standard open jet wind tunnel mentioned earlier.

Rough sandpaper was applied near the nozzle outlet to establish early transition of the boundary layer. For the unsteady wall pressure and boundary layer velocity measurements, two types of flat plate models were used. The first model has a straight trailing edge. The flow surface is flat up to the trailing edge, and a small bevel angle is present at the back side to allow a gradual tapering across the total plate thickness of 5 mm. Note that there is no flow at the back side of the test model. Another flat plate model has a serrated sawtooth trailing edge with the following specifications: root-to-tip distance ($2h$)=20 mm, and a serration angle (φ)=25°, where the symbols are explained in Fig. 1. Similarly, a small bevel angle is present near the trailing edge at the back side where no flow is present.

There are 34 microphone ports near the trailing edges of each flat plate model. Each port is 0.5 mm in diameter and 1 mm deep, which is followed by a recess hole inside the flat plate of 1 mm diameter. The depth of the recess hole is different, depending upon the location with respect to the trailing edge. The recess holes are used to hold a small metal tube of 0.5 mm internal diameter, which will be connected to a plastic tube as part of a remote microphone system. As shown in Fig. 1, these sensing holes are named individually and distributed in identical rectilinear grids for both of the straight and serrated sawtooth trailing edges. This configuration allows the wall pressure *PSD* and streamwise, spanwise and oblique coherence functions to be compared directly between the straight and serrated sawtooth trailing edges. Note that the wall pressure *PSD* was measured sequentially by a single microphone on the 34 microphone ports, whilst the coherence functions were obtained by simultaneous acquisition from two microphones.

A third test model, namely the heater plate, is manufactured for the thermochromic liquid crystal flow visualization experiment. The experiment was carried out in a non-isothermal condition, where the flat plate test model was heated up slightly. For this purpose a heater flat plate is designed from a 150 mm × 295 mm printed circuit board (PCB). The PCB comprises an etched copper track in a non-metallic substrate. As shown in Fig. 2, the tortuous, single-filed copper track in a V-shape pattern is connected to a direct current (DC) power supply to heat up the main part of the plate surface, as well as the sawtooth region of the serrated trailing edge. During the experiments, the substrate side of the PCB is used as the flow surface to allow better heat dissipation. A 0.2 mm thick plastic film was attached to the substrate surface, followed by spraying the plastic film with matt-black paint before an artist airbrush was used to spray the liquid crystal evenly to the matt-black surface. In order to minimize heat loss by conduction, a 75 mm thick Styrofoam sheet was attached to the non-flow surface, which is the copper-track face of the PCB. The PCB heater plate has the same sawtooth trailing edge configuration of $2h$=20 mm and φ=25°.

In order to change from a serrated sawtooth trailing edge to a straight trailing edge in the heater plate, several add-on triangular plates are inserted to the gap between adjacent members of the sawtooth to form a continuous and uniform surface across the span. The maximum step height as the result of attaching the add-on triangular plates to the sawtooth trailing edge is estimated to be less than 0.1 mm. This corresponds to $y^+ \approx 8$ near the trailing edge, where y^+ is the normal distance in the wall unit. This small protuberance with relative to the viscous sublayer is not expected to alter the characteristics of the turbulent boundary layer significantly. Note that this add-on method is only applicable to the liquid crystal experiment.

2.2. Experimental methods

2.2.1. Liquid crystal technique

Optically active (chiral nematic) liquid crystals have a naturally twisted structure that is formed by different layers of molecules. The twisting structure provides an unusual optical property which is called a selective reflection. In this case only incidence light with a specific wavelength equal to the crystal pitch will be reflected. When liquid crystal is applied to a test surface in a thin coat, the pitch of the helical structure in the crystals can be made to change to respond solely to the variation in surface temperature. Once the surface heat flux is known, the heat transfer rate can be obtained [18]. The coating techniques, illumination and viewing angles and calibration technique will be discussed here.

The liquid crystal slurry and binder were supplied by Hallcrest Ltd. According to the specification, the liquid crystal has an active color bandwidth of about 10 °C, with visible red color starting at approximately 25 °C through the visible spectrum to blue at 35 °C. During preparation, 4–5 coatings of the mixture of the crystal slurry and binder were sprayed on the matt-black painted surface of the heater plate. As stated by Baughn [19], poor color display will result if the coating is either too thin or too thick. The amount of the mixture was estimated beforehand. Based on mass conversion and losses estimation through spraying, the thickness of the nominal coating is estimated to be about 30 μm.

A 60 W fluorescent strip light that has approximately the same length as the test plate was used to illuminate the liquid crystal surface. It was found that the optimum viewing angle is approximately perpendicular to the coating surface. The

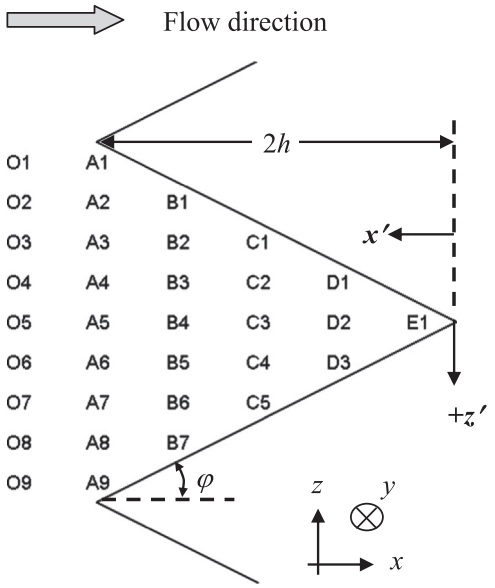

Symbol	$x'/2h$	$z'/2h$
E1	0.1	0
D1	0.3	-0.1
D2	0.3	0
D3	0.3	0.1
C1	0.5	-0.2
C2	0.5	-0.1
↓	↓	↓
C5	0.5	0.2
B1	0.7	-0.3
B2	0.7	-0.2
↓	↓	↓
B7	0.7	0.3
A1	0.9	-0.4
A2	0.9	-0.3
↓	↓	↓
A9	0.9	0.4
O1	1.1	-0.4
O2	1.1	-0.3
↓	↓	↓
O9	1.1	0.4

Fig. 1. Distribution of the microphone sensing holes on the sawtooth trailing edge. Same arrangement of the microphone sensing holes also applies to the baseline, straight trailing edge. The coordinates of the sensing holes are tabulated in the table.

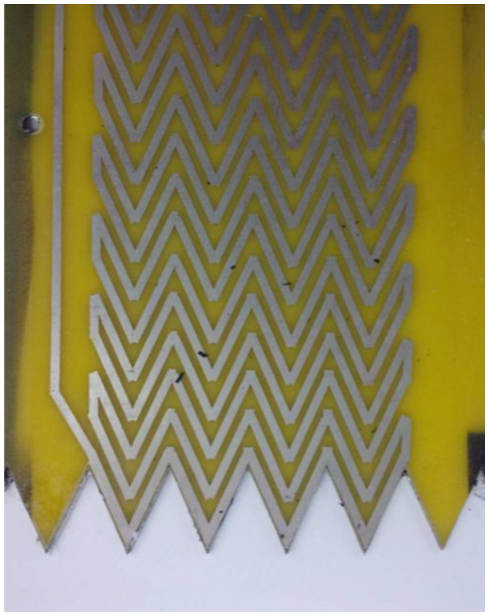

Fig. 2. The PCB heater flat plate with a specially designed copper track for the liquid crystal experiment.

images were captured by a digital camera. The illumination arrangement and camera position are kept exactly the same during the calibration and measurement.

The variation of the liquid crystal color was calibrated against the surface temperature, which was measured by a K-type glue-on type thermocouple. The electrical power for heating the test surface is controlled by a DC power supply. The current is adjusted to raise the surface temperature in a number of steps. For each electrical power input value, picture of the liquid crystal will only be taken after a steady state temperature has been indicated. This process is repeated until the maximum liquid crystal activation temperature has passed. In this way, the visible color spectrum of the liquid crystal is fully utilized. The temperature resolution for the calibration curve is about 0.3 °C.

After the calibration, the recorded pictures are converted from *Red*, *Green* and *Blue* (RGB) color indices to *Hue*, *Saturation* and color *Intensity* (HSI) indices. It was found that the *Hue* exhibits the best sensitivity to the temperature. The interrogation area in the digital image is selected to be the area encompassing the location near the thermocouple, where a mean *Hue*

value is calculated for each temperature reading. The *Hue*–temperature relationship pertaining to the current experiment is shown in Fig. 3. From the figure, steeper gradients occur at temperatures between 25 and 27 °C. Above this range the variation of *Hue* with respect to the temperature becomes more gradual. It was found that the *Hue* value displayed by the liquid crystal actually continues to increase beyond the saturated temperature specified by the company. A lookup table method was employed to convert the liquid crystal's *Hue* value to the surface temperature. More information on the liquid crystals techniques can be found in Zhong et al. [20] and Vathylakis and Chong [21].

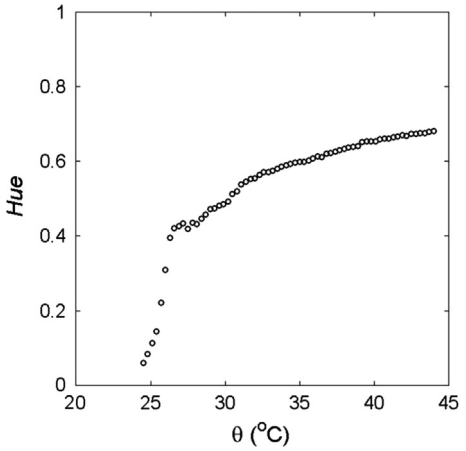

Fig. 3. *Hue*–temperature calibration curve for the thermochromic liquid crystal.

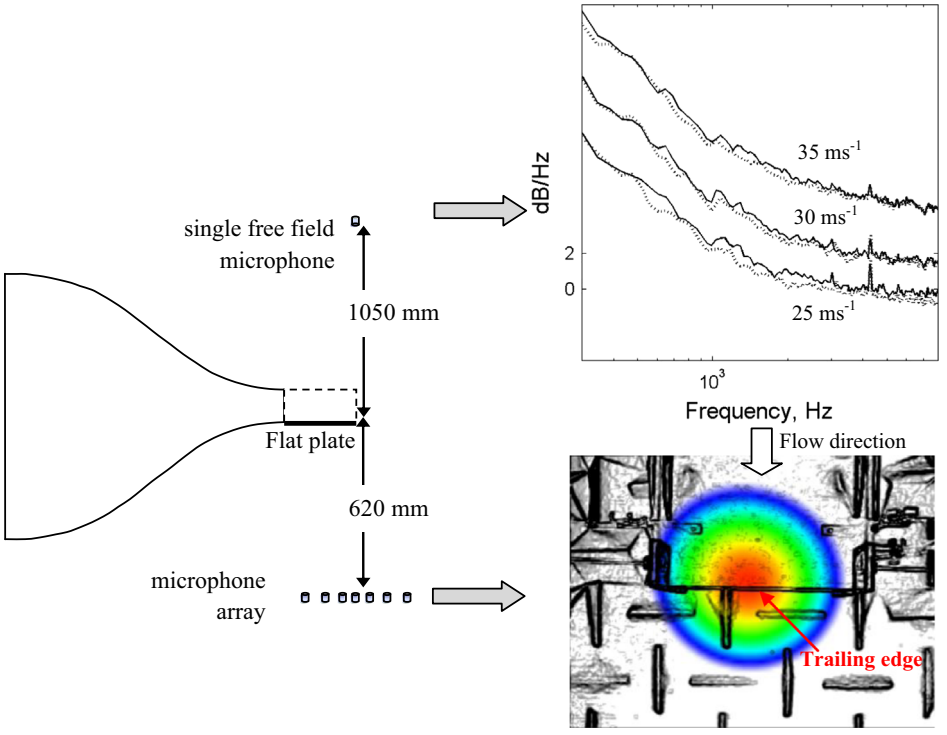

Fig. 4. Experimental setup for the measurements of self noise produced by flat plate fitted in turn with a straight trailing edge and a serrated trailing edge. Noise spectra produced by straight trailing edge (—) and serrated sawtooth trailing edge (· · · ·) at freestream velocities of 25, 30 and 35 m s^{-1} are measured by the single free field microphone. The microphone array is used to locate the noise source.

2.2.2. Far field microphone and near field remote microphones

For the far field noise measurement, a $\frac{1}{2}$ in. pre-polarized condenser microphone (LarsonDavis 377B02) was placed 1.05 m above the trailing edge at mid span and at a polar angle of 90°, as shown in Fig. 4. The noise data was sampled at 44 kHz by a 16-bit analog-to-digital (A/D) card from the National Instrument (A/D) card from the National Instrument. The far field acoustic data was windowed-FFT and averaged to obtain the *PSD* with a 1 Hz resolution in bandwidth.

The near field wall pressure measurements utilized the same type of microphone. Single microphone was used to measure the wall pressure *PSD*, whilst a pair of microphones was simultaneously used to measure the coherences of the unsteady wall pressure near the trailing edges of the flat plate. The microphone ports are 0.5 mm in diameter which should give satisfactory spatial resolution of the measured pressure and minimal attenuation of eddies with small wavelength. The microphones are connected to the sensing holes via a remote system. The microphone is always positioned directly underneath the sensing hole so that a straight line of sight can be drawn from the center of the sensing hole, via a straight plastic tube (0.5 mm internal diameter and 10 mm long), and into the center of the microphone. Owing to the minimal sudden area change along the tube duct, and the relatively short plastic tube, strong acoustic resonance in the form of traveling waves is not very significant in this particular remote arrangement. Because the backside of the test plates is not exposed to any flow, there is a large degree of freedom in positioning the remote microphone system outside the wind tunnel. Unlike the embedded microphone method, the current remote microphone arrangement allows the wall pressure measurements to take place very near to the edges.

In this study no magnitude calibration of the two microphones was performed in the remote configuration. Considering that the main objective of this paper is to investigate the difference of unsteady wall pressure *PSD* levels between the straight trailing edge and serrated sawtooth trailing edge, and that the same microphone was used throughout the experiment, an absolute magnitude in wall pressure is not necessary. However, phase calibration between two microphones used in the coherence measurements had been performed. During the phase calibration, both the microphones in remote configuration were connected to ports O5 and O6 respectively (see Fig. 1). A loudspeaker calibrator, driven by a white noise signal input, is then used to provide identical sound waves to both the pressure ports. A good coherence between the microphone signals is obtained and the phase angles are small within a wide frequency range. During the acquisition of the unsteady wall pressure, the sampling frequency and sampling time were set at 44 kHz and 10 s, respectively. The digitization of the analog signals was performed by a 16-bit National Instrument A/D card. The wall pressure data was also windowed-FFT and averaged to obtain the *PSD* with a resolution of 1 Hz bandwidth.

2.2.3. Acoustic beamformer

A conventional delay-and-sum beamformer manufactured by GFAI Tech GmbH with a 0.35 m diameter carbon-body planar ring array consisting of 32 microphones was used to beamform the noise source radiated from the flat plate. The microphones are electrets type of $\frac{1}{4}$-in. diameter (Sennheiser model 4211). The frequency response of the microphones is 20 Hz–20 kHz ($\pm$ 3 dB) with a dynamic range of 28–130 dBA. An integrated fixed focus camera is placed in the middle of the round array. The acoustic mapping data is acquired through a 24-bit data recorder with a sampling rate up to 192 kHz per analog channel. As shown in Fig. 4, the array was placed on a tripod where its center pointed upwards, focusing on the trailing edge of the flat plate at a distance of 0.62 m and a polar angle of –90°. The noise data was sampled at 48 kHz for 32 s, which was then windowed (Hamming) to estimate the *PSD* of 1 Hz bandwidth using 1024 point FFT.

2.2.4. Hot wire anemometry

In order to determine the turbulence structure on the flat plate surface, a miniature type X-wire (DANTEC 55P61) was used to measure the two-component velocity fluctuations u' and v'. The diameter and length of each wire are 5 μm and 1.25 mm respectively. The X-wire was operated at an overheat ratio of 1.6. It is known that a high overheat ratio is generally preferable in order to maintain a high velocity sensitivity. However, when the flow speed is low (e.g. the probe is close to the wall surface), the natural thermal convection from one particular wire to another, and vice versa, could potentially lead to error in the velocity readings. This phenomenon is known as the "cross-talk". For identification of the individual wire in the X-wire probe, they are labeled as (X-a) and (X-b), respectively. To determine the level of "cross-talk" in our experiment, the X-wire probe was placed at a freestream velocity of about 1 m s^{-1}. In the first step, wires (X-a) and (X-b) were switched off and on, respectively. After the mean voltage from the wire (X-b) was recorded, the second step is to switch both wires (X-a) and (X-b) on. Voltage reading for wire (X-b) was again taken whilst the freestream velocity of 1 m s^{-1} remains unchanged. It is found that the discrepancy between readings for the wire (X-b) is less than 3%. Similar level of discrepancy is obtained when the above procedure is repeated with the wires alternated.

A full velocity versus yaw-angle calibration technique [22] was employed to convert the acquired voltages into the velocities. This calibration method reduces the potential error incurred by the different sensitivity of the yaw coefficients to the velocity. The data was sampled at a frequency of 20 kHz for approximately 26 s at each point by a 12-bit A/D card (TSI ADCPCI). Due to the orientation of the X-wire with respect to the wall surface, the closest measurement point to the wall surface is about 1 mm. Because the test plate is made from a non-metallic material, near wall correction for the X-wire probe at this height might not be necessary. The probe was attached to a computer controlled two-dimensional traverse system that can achieve an accuracy of 0.01 mm in each direction.

A triple-sensor hot wire probe (TSI-1299) was used to measure the three-velocity components in the wake flow. The conversion of the acquired voltage signals to the velocities is by the algorithm developed by Lekakis et al. [23].

3. Aeroacoustic results

Fig. 4 shows the far field noise measured over the flat plate fitted in turn with a straight trailing edge and a serrated sawtooth trailing edge ($2h=20$ mm, $\varphi=25^\circ$). Across a fairly broad frequency range, the acoustic *PSD* measured at 25, 30 and 35 m s^{-1} demonstrate that the serrated sawtooth trailing edge consistently produces 0.5–1.0 dB lower noise levels when compared to the noise spectra produced by the straight trailing edge. For clarity, the background noise (without the flat plate) for each velocity case is not shown in the figure, but they are all at least 3 dB lower than the noise level produced by the flat plate.

A microphone beamformer is positioned as per the illustration in Fig. 4 to locate the noise source. Acoustic beamforming was carried out when the free jet velocity is at 30 m s^{-1}. Noise reduction is dominant at the frequency range of $1<f<2.5$ kHz. This frequency range is therefore chosen as the interrogation range for the beamforming. The result demonstrates that the radiated noise at the frequency range where reduction occurs is originated from the trailing edge of the flat plate. Both the hardware setup and the ambient conditions are exactly the same between the experiments for the flat plate with straight trailing edge and the flat plate with serrated sawtooth trailing edge. Geometrical modification of the trailing edge from straight to serration is therefore the main reason where noise reduction is observed in the results.

Some theories [12,24] assume a full Kutta condition at the trailing edge when formulating expression for the far field noise. The current flat plate configuration means that flow is only present on one side of the surface. The radiated self noise level will be lower than when there is flow on both sides of the surface, though the spectral shape is not expected to be significantly different. This explains the smaller amount of broadband noise reduction achieved by serrated sawtooth trailing edge in the current flat plate configuration compared to an airfoil, where a broadband noise reduction between 3 dB and 7 dB is reported [8–11].

4. Wall heat transfer on a serrated trailing edge

A good contrast in color display by the liquid crystal is predominantly found in inhomogeneous fluid flows such as the transitional boundary layer or laminar separation. In the present study, the boundary layers for both the straight trailing edge and serrated sawtooth trailing edge are already in a turbulent state. Turbulent separation is also not likely to occur on the flat plate. As a result, the variation of the turbulent heat transfer, which could potentially restrict the color range over which the liquid crystals can effectively display temperature differences, was initially not expected to be too significant. However, as will be shown later, some interesting features are clearly displayed by the liquid crystals on the serrated sawtooth trailing edge.

The wall surface was only heated slightly and the characteristics of the turbulent boundary layer will not be modified by a considerable amount. Once heated, a long setting time is allowed to ensure that the wall temperature always reaches a saturated state across the whole plate surface. The sequence of experiments will normally begin with the straight trailing edge first, where several add-on inserts were already attached. After photos were taken, the add-on inserts will be removed in situ as quickly as possible to change the trailing edge into a serrated sawtooth type. It is important to note that during this short interval the room temperature and flow condition do not change considerably. Therefore a simple comparison with the surface temperature between the straight trailing edge and the serrated sawtooth trailing edge will be sufficient.

Raw liquid crystal images of the straight and serrated sawtooth trailing edges were taken under exactly the same flow conditions, the same amount of heating in the PCB and the same ambient temperature. After the whole surface temperature maps are calculated for the straight and serrated sawtooth trailing edges, contour map showing the temperature difference $\Delta\theta\,(x,z)=\theta_{\text{serration}}\,(x,z)-\theta_{\text{straight}}\,(x,z)$, where θ is the wall temperature, can then be obtained. The result is shown in Fig. 5. Note that a negative $\Delta\theta$ value means that the serrated sawtooth has a lower temperature than the unserrated, straight case

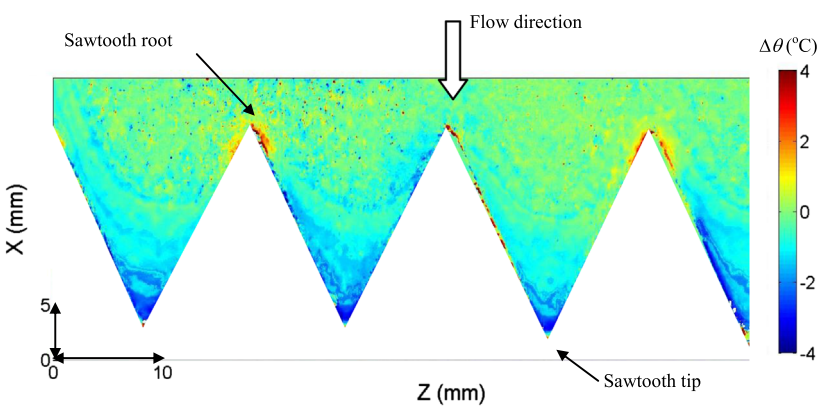

Fig. 5. Surface contour map of $\Delta\theta$ (°C) obtained by the liquid crystal technique. The geometrical parameters for the serrated sawtooth trailing edge is $2h=20$ mm and $\varphi=25^\circ$.

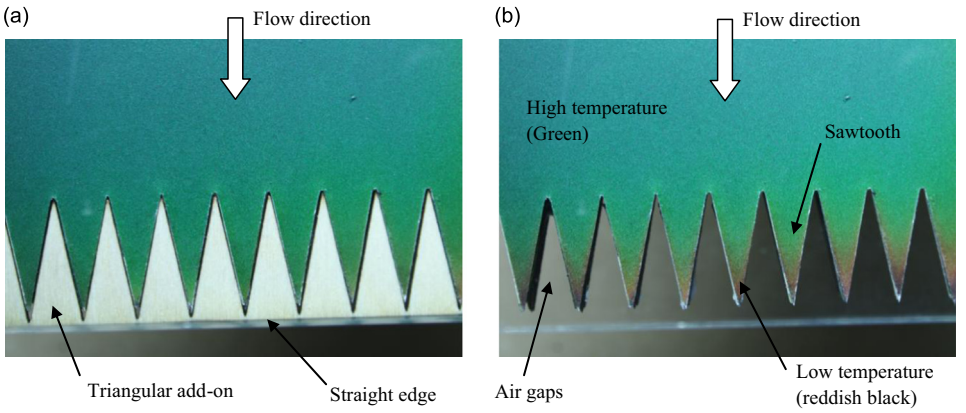

Fig. 6. Raw thermochromic liquid crystal images for the (a) straight trailing edge and (b) serrated sawtooth trailing edge (narrower angle), with $2h=20$ mm and $\varphi=12.5^\circ$. (For interpretation of the references to color in this figure, the reader is referred to the web version of this article.)

at the same location. The opposite is true for the positive $\Delta\theta$. Since the non-isothermal condition in the current study is achieved by heating the test object in cold air, a lower surface temperature implies that the convective heat transfer rate is higher. Therefore, the lower temperatures on the sawtooth side edges and the sawtooth tips clearly indicate the presence of higher convective heat transfer rates there.

A second test was performed on another heater plate of the same overall dimension, but the trailing edge of this heater plate has a smaller serration angle of $\varphi=12.5^\circ$ while the root-to-tip distance is maintained at $2h=20$ mm. The raw images of the liquid crystal for the straight and serrated sawtooth trailing edges, where both were subjected to the same flow condition, same ambient temperature and same amount of heating to the PCB, are presented in Fig. 6. Note that we only show the raw liquid crystal images because the reddish-black color exhibited by the sawtooth tip region in Fig. 6b is out of the *Hue*–temperature calibration range, thus it is not effective to present the $\Delta\theta$ contour. Nevertheless, the raw liquid crystal images are still very vivid, where the narrower-angle serration demonstrates that lower surface temperature (higher heat transfer) exists near the sawtooth side edges and sawtooth tips. It is also observed that the percentage of low temperature region occupying each sawtooth is greater than that in a wider-angle serration as shown in Fig. 5. The implication of this will be discussed in Section 7.

Based on the two liquid crystal results, higher heat transfer rates near the side edges and tips of the serrated sawtooth trailing edge are clearly demonstrated. This suggests that a convective regime, which is much stronger than a two-dimensional turbulent boundary layer, should exist for a serrated sawtooth trailing edge. Supported by further experimental evidences which will be discussed later, we believe that the low temperature region near the sawtooth side edge is caused by a convective pressure-driven vortical structure. The much lower temperature near the sawtooth tip is probably caused by the amalgamation of the vortical structures on both sides.

5. Unsteady wall pressure on a serrated trailing edge

5.1. Power spectral density of wall pressure

Using the methodology described in Section 2.2.2, a comparative study is performed for the wall pressure *PSD* produced by the straight and serrated sawtooth trailing edges. As shown in Fig. 1, the measurement points comprise 34 locations of O1–O9, A1–A9, B1–B7, C1–C5, D1–D3 and E1 for both trailing edges. Note that the locations O1–O9 are situated upstream of the sawtooth roots.

The following quantity is introduced:

$$\Delta\eta(x,z,f)=10\log_{10}\left[\frac{\overline{P}'^2_{\text{straight}}(x,z,f)}{\overline{P}'^2_{\text{sawtooth}}(x,z,f)}\right], \tag{1a}$$

where $\overline{P}'^2(x,z,f)$ is the mean square pressure fluctuations at each measurement point of either the straight or the serrated sawtooth trailing edges. $\Delta\eta\,(x,z,f)$ thus represents the difference in wall pressure *PSD* level between the two trailing edges in the x–z plane at a particular frequency. A negative $\Delta\eta$ value denotes that the wall pressure *PSD* for the serrated sawtooth is higher than the unserrated, straight case at the same location. The opposite is true for the positive $\Delta\eta$ value. When the wall pressure *PSD* is integrated across the frequency range, an overall spectral energy level roughly equal to the root-mean-square value is obtained. Accordingly, another comparative quantity $\Delta\varepsilon\,(x,z)$ can be defined

$$\Delta\varepsilon(x,z)=10\log_{10}\left[\frac{\int_{f\in J}\overline{P}'^2_{\text{straight}}(x,z,f)\mathrm{d}f}{\int_{f\in J}\overline{P}'^2_{\text{sawtooth}}(x,z,f)\mathrm{d}f}\right]. \tag{1b}$$

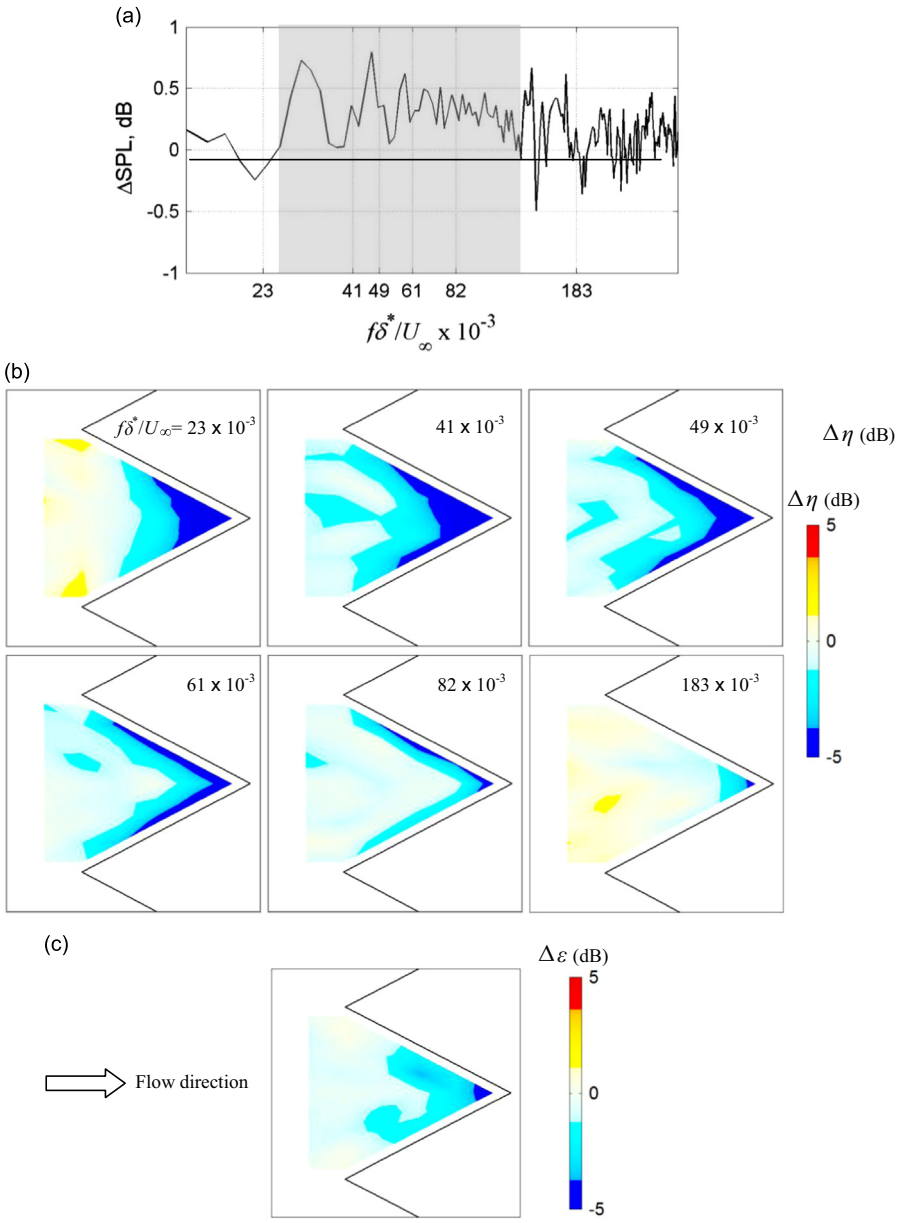

Fig. 7. (a) ΔSPL (dB), (b) contour maps of $\Delta\eta$ (dB) at different Strouhal numbers, and (c) contour map of $\Delta\varepsilon$ (dB) integrated over $J=(97, 21{,}950)$ Hz. Note that all the figures in (a), (b) and (c) correspond to the same free jet velocity of 30 m s^{-1}.

Previously in Section 3, it has been shown that small level of noise reduction can be achieved by the serrated sawtooth trailing edge in a flat plate configuration. Fig. 7a represents the difference in sound pressure level (ΔSPL) between a straight and a serrated sawtooth trailing edge at 30 m s^{-1} free jet velocity. The positive ΔSPL denotes noise reduction, and the opposite is true for the negative ΔSPL.

The frequency in Fig. 7a is represented by the Strouhal number ($f\delta^*/U_\infty$), where δ^* is the boundary layer displacement thickness at a reference location C3 measured directly inside the aeroacoustic wind tunnel facility, and U_∞ is the local freestream velocity. The non-dimensionalization of the frequency is to enable comparison with the wall pressure *PSD* in Fig. 7b, which was obtained in a separate wind tunnel. Similarly, Strouhal number $f\delta^*/U_\infty$ is used to represent the frequency in Fig. 7b, where the δ^* was also measured in situ at location C3. Note that the overall dimension of the flat plates used for the aeroacoustic and aerodynamic tests, including their sawtooth geometries, are exactly the same. The discrepancies of the measured U_∞ and δ^* between both tests are 1.3% and 9.6%, respectively. The use of Strouhal number could therefore minimize the margin of error when comparing the flow and acoustic results.

In Fig. 7a, the ΔSPL fluctuates around the zero level at $f\delta^*/U_\infty \geq 0.126$. However, at $0.027 < f\delta^*/U_\infty < 0.126$ (indicated by the shaded region), a clearer pattern of noise reduction can be identified. Contour maps of $\Delta\eta$ at $f\delta^*/U_\infty = 0.023$, 0.041,

0.049, 0.061, 0.082 and 0.183 are shown in Fig. 7b. At $f\delta^*/U_\infty = 0.023$, where noise reduction by the serrated sawtooth trailing edge is not yet fully established, the dominant *PSD* level for the wall pressure is concentrated around the sawtooth tip only. At $0.041 \leq f\delta^*/U_\infty \leq 0.082$, where noise reduction is observed, the dominant *PSD* level for the wall pressure seems to diffuse from the sawtooth tip towards the upstream direction along the sawtooth side edges. At $f\delta^*/U_\infty = 0.183$, where noise reduction ceases to exist, the wall pressure *PSD* level for the serrated sawtooth becomes almost similar to the unserrated, straight trailing edge ($\Delta\eta \approx 0$). The above comparison between the acoustic spectral and wall pressure spectral suggests that the reduction in noise radiation should be accompanied by the co-existence of a high *PSD* level in wall pressure at the sawtooth side edges and the sawtooth tip.

When the wall fluctuating pressure is integrated across $J = (97, 21{,}950)$ Hz in Eq. (1b), the resulting $\Delta\varepsilon$ contour in Fig. 7c also produces high spectral energy levels at location close to the sawtooth side edges and the sawtooth tip. The wall pressure spectral energy distribution thus correlates very well with the liquid crystal results ($\Delta\theta$) presented in Section 4.

We note the possible effect of acoustical back-scattering. In this case the total wall pressure measured by microphones near the sawtooth side edge and the sawtooth tip could include both the incidence pressure and the scattered pressure. Moreover, the total wall pressure measured near the sawtooth tip could be amplified further by the multiple back-scattering of acoustic waves from the two side edges. Because the effect of acoustical back-scattering is frequency-dependent with the largest decay rate occurring at high frequencies, the integration of the measured wall pressure across a whole range of frequencies in Eq. (1b) should help to reduce this effect. In addition, the boundary layer incidence pressure is understood to be considerably larger in magnitude than the scattered pressure [25]. Most important, the variations of $\Delta\varepsilon$ in Fig. 7c are found to be highly correlated with the $\Delta\theta$ contour map in Fig. 5. It is important to note that the $\Delta\theta$ contour will not be affected by the acoustical back-scattering at all. Therefore the hypothesis of strong turbulence/vortical fluctuations near the sawtooth side edge and the sawtooth tip is still valid. This issue will be further addressed in Section 6 when the cross spectral density distribution between the boundary layer velocity fluctuations and the unsteady wall pressure, as well as the characteristics of momentum/turbulence transports in time domains, are analyzed.

5.2. Streamwise and spanwise coherence and phase functions

The results in the previous section were obtained by a single microphone. In order to investigate the coherences γ^2 and phases ϕ of the turbulent eddies, a pair of microphones in various combination of Δx (streamwise spacing) and Δz (spanwise spacing) was used to measure the unsteady wall pressures simultaneously for both the straight and serrated sawtooth trailing edges. Although large amount of data were obtained, only selective results are presented here for clarity. Fig. 8 shows the phase spectra for the streamwise arrangement of microphones (i.e. $\Delta x > 0$, $\Delta z = 0$). Note that the pairing of the microphones is identified using the notations in Fig. 1. For example, if one microphone is located at the sawtooth tip and another one at 4 mm behind it, then this pairing will be written as D2–E1. The same principle applies throughout the paper. Note that drawings are also included in the figure to illustrate the locations of the pairing.

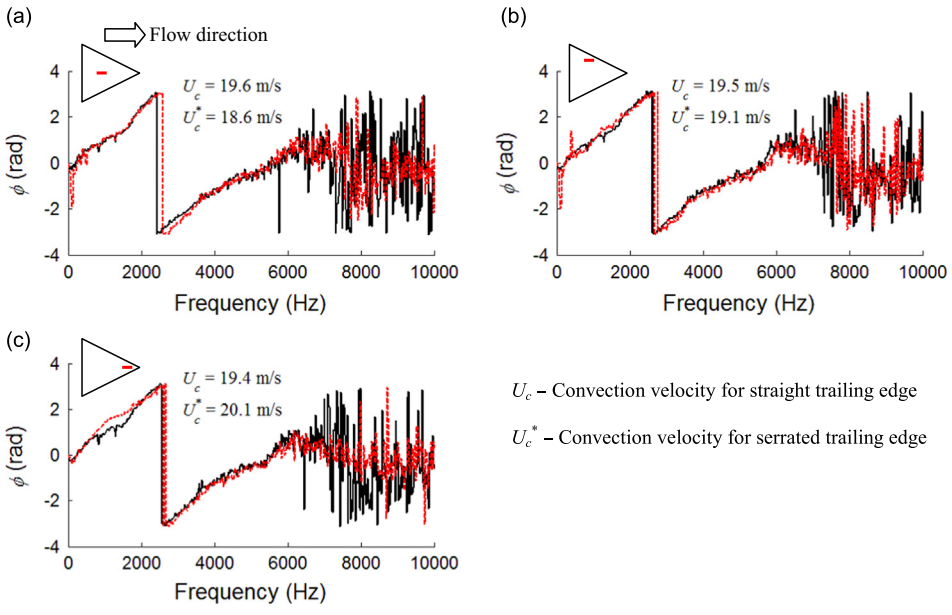

Fig. 8. Streamwise phase spectra ϕ (radian) for the straight (black) and serrated sawtooth (red) trailing edges of the following microphone pairs: (a) B4–C3; (b) B2–C1; and (c) D2–E1. (For interpretation of the references to color in this figure legend, the reader is referred to the web version of this article.)

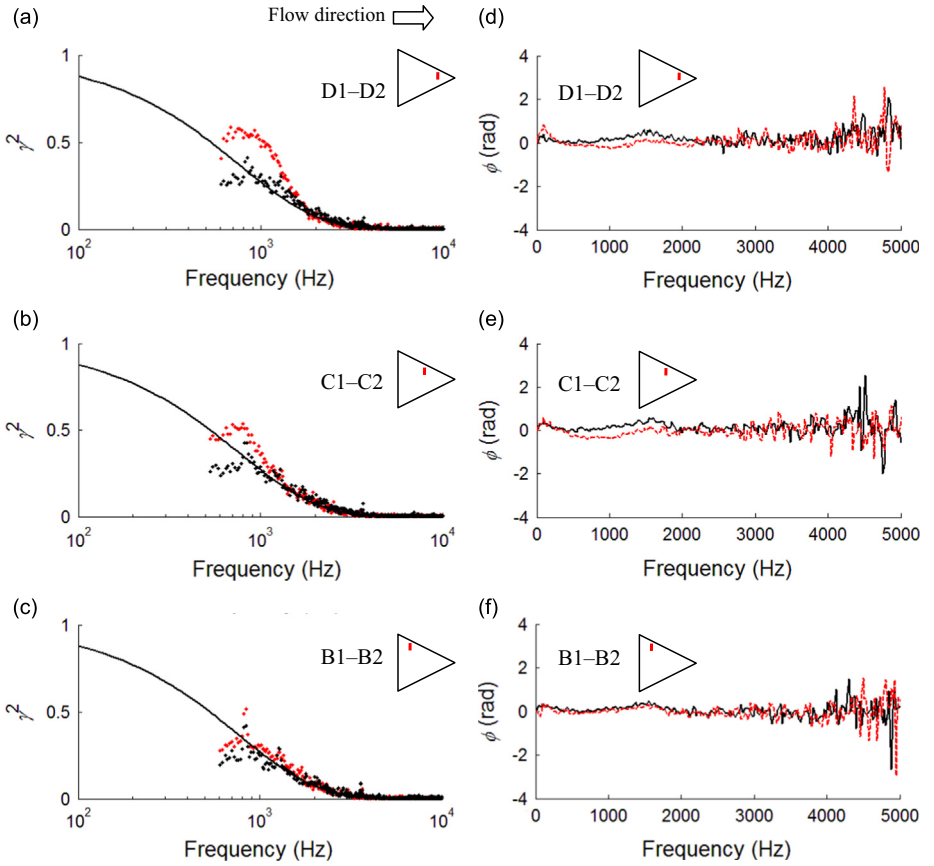

Fig. 9. (a–c) Spanwise coherence γ^2 (● straight trailing edge, ● serrated trailing edge) and (d–f) phase spectra ϕ (— straight trailing edge, - - - serrated trailing edge). The solid lines in the coherence γ^2 plots are calculated from the empirical model by Brooks and Hodgson [25]. (For interpretation of the references to color in this figure legend, the reader is referred to the web version of this article.)

The phase spectra can be further implemented for the calculation of the turbulence convection velocity U_c by

$$U_c = 2\pi\Delta l\frac{\mathrm{d}f}{\mathrm{d}\phi}. \tag{2}$$

For ($\Delta x > 0$ and $\Delta z = 0$), $\Delta l = \Delta x$. The calculated convection velocities are included in Fig. 8. It is generally observed that the turbulent eddies propagate at a similar speed in the streamwise direction regardless of the type of trailing edge used. This observation also applies to the case when the microphone pair is close to the sawtooth side edge (e.g. B2–C1) and the sawtooth tip (e.g. D2–E1) where stronger turbulence activities have been identified previously for a serrated sawtooth trailing edge.

Some spanwise coherence spectra (i.e. $\Delta x = 0$, $\Delta z > 0$) are presented in Fig. 9a–c for the following cases: D1–D2, C1–C2 and B1–B2. The corresponding phase spectra are also shown in Fig. 9d–f. The measured coherences in the spanwise direction are compared with an empirical model [25]:

$$\gamma^2(f) = \exp\left(-\frac{2\pi f}{bU_c}\Delta z\right), \tag{3}$$

where b is the Corcos constant and the value is adjusted to best-fit with the measured spanwise coherence spectra. In the current study, the adjustment is made against the measured coherence function for the straight trailing edge and it was found that a value of 0.5 fits well for all the straight trailing edge cases. Some interesting features can be observed for the serrated sawtooth trailing edge. The measured spanwise coherences at the region near the sawtooth tip (i.e. D1–D2) are higher and do not fit well with the empirical curve until about 2 kHz. This trend is also repeated at the upstream location C1–C2, although the difference in coherence spectra level between the straight and serrated sawtooth trailing edges becomes smaller. At an even further upstream location B1–B2, there is no longer any discernible difference between the straight and serrated sawtooth trailing edges. The above phenomena are also reflected in the corresponding phase spectra. The microphone pairs D1–D2, C1–C2 and B1–B2 are all in phase (i.e. $\phi \approx 0$) for the straight trailing edge, which indicates that there is almost no turbulence convection in the spanwise direction. However, with the exception of the B1–B2 case, the microphone pairs of D1–D2 and C1–C2 for the serrated sawtooth trailing edge are not exactly in phase at frequencies below

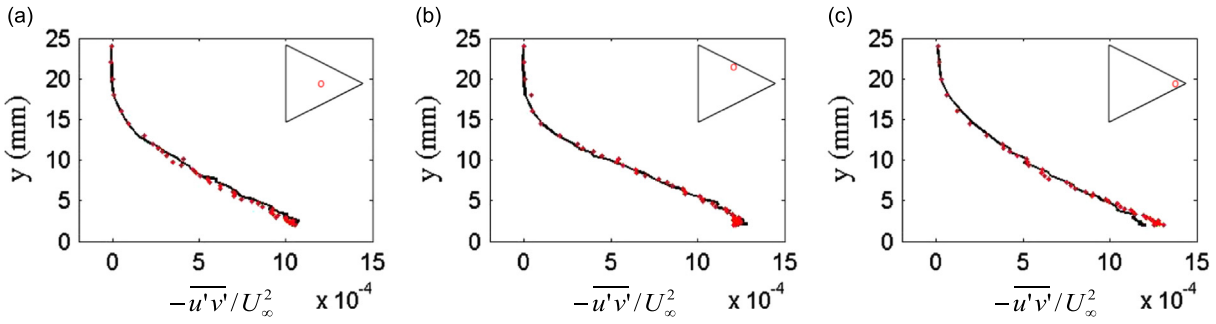

Fig. 10. Time-averaged Reynolds shear stresses $-\overline{u'v'}/U_\infty^2$ boundary layer profiles measured at locations (a) C3, (b) C1, and (c) E1 for both of the straight (—) trailing edge and serrated sawtooth (●) trailing edge. (For interpretation of the references to color in this figure legend, the reader is referred to the web version of this article.)

2 kHz. Based on the earlier observation of stronger turbulence activities near the sawtooth side edges, and the spanwise coherences and phase functions presented in this section, there is a strong indication that the significant turbulence activities are associated with a vortical flow, which probably originates at a location close to C1 at the sawtooth surface.

Measurements are also performed for microphone pairs with both streamwise and spanwise separations (i.e. $\Delta x > 0$, $\Delta z > 0$). The associated phase spectra are also used to determine the turbulence convection speeds. The results will be discussed in Section 7.

6. Turbulent boundary layer developed on a serrated sawtooth trailing edge

The previous sections concern the steady and unsteady *near wall* properties of the straight and serrated sawtooth trailing edges. To provide a better understanding of the mechanisms involved, boundary layer measurements were performed at locations C1, C3 and E1 to investigate the time-averaged Reynolds shear stresses, power spectral densities, cross spectral densities and conditionally-averaged velocity perturbations, velocity fluctuations and Reynolds shear stresses. Note that the wall pressure data was also acquired simultaneously with the X-wire during each measurement. The wall pressure data will be used for the velocity–pressure cross spectral density analysis in Section 6.1, and will also act as a reference signal for the boundary layer velocity conditional-averaging in Section 6.2.

6.1. Time-averaged turbulence quantities

Boundary layer profiles of Reynolds shear stress $-\overline{u'v'}/U_\infty^2$ are shown in Fig. 10. As shown in the embedded drawing, C3 is located at $x=h$ from the trailing edge (the total length of the sawtooth is $2h$) and in the plane of symmetry of the sawtooth. At this location there is no noticeable difference in the Reynolds shear stress between the straight and serrated sawtooth trailing edges (Fig. 10a). This result corresponds well with the surface temperature obtained by the liquid crystal techniques and the unsteady wall pressure *PSD* contour maps. These measurements demonstrate that the area in the vicinity of C3 is isolated from the side edge vortical structures. C1 is also located at $x=h$ from the trailing edge, but near the side edge of the sawtooth (see the embedded drawing in Fig. 10b). Based on a qualitative assessment of the surface temperature and the unsteady wall pressure spectral contour maps, location C1 is just about to submerge into the side edge vortical structures. Although the time-averaged Reynolds shear stress profiles between the straight trailing edge and serrated sawtooth trailing edge are similar (Fig. 10b), difference still exists for the dynamic momentum transfers and turbulence transports at C1. This will be discussed further in the next section.

E1 is situated near the sawtooth tip, as demonstrated in the embedded drawing. The local turbulent boundary layer at this location is expected to interact strongly with the oblique vortical structures. This is manifested in Fig. 10c where a slightly higher (up to 8% difference) turbulence shear stress level is observed at the near wall region of the serrated sawtooth trailing edge. The power spectral densities of the velocity fluctuating components $\Phi_{u'}$ and $\Phi_{v'}$ are also examined and the results are shown in Fig. 11. For the serrated trailing edge at location E1, both the $\Phi_{u'}$ and $\Phi_{v'}$ in Fig. 11c exhibit spectral humps with a central frequency occurring at a Strouhal number ($f\delta^*/U_\infty$) of about 0.045 at $y/\delta^* \approx 1.7$. Note that the same Strouhal number also corresponds to the maximum level of noise reduction as demonstrated in Fig. 7a. The existence of velocity spectral humps in the boundary layer provides further evidence that vortical structures can be produced by a serrated sawtooth trailing edge, and they are totally absent in a straight trailing edge. At locations C3 and C1, as shown in Fig. 11a and b respectively, the $\Phi_{u'}$ and $\Phi_{v'}$ remain similar between the straight and serrated sawtooth trailing edges, where no velocity spectral hump is found.

Further analysis on the cross spectral density is attempted to establish a relationship between the product of the two-component velocity fluctuations ($u'v'$) and the surface pressure fluctuation p'. The cross spectral density provides information about the flow features responsible for the wall pressure generation. Fig. 12 shows the cross spectral density $\Phi_{(u'v'),p'}$ near the tip of the sawtooth (E1). Note that the level is in decibel. For the serrated sawtooth trailing edge in Fig. 12b,

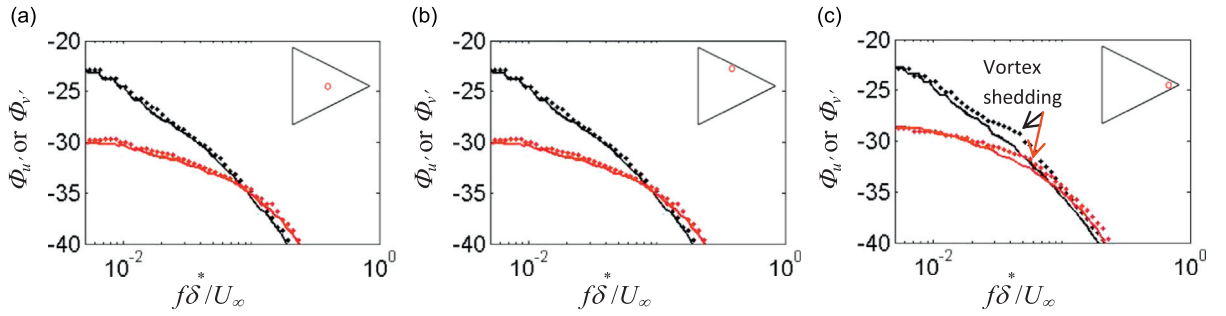

Fig. 11. Comparison of the fluctuating velocity power spectral densities of $\Phi_{u'}$ and $\Phi_{v'}$ at $y/\delta^* \approx 1.7$ for locations (a) C3, (b) C1, and (c) E1, between the straight trailing edge and serrated sawtooth trailing edge. Explanation of symbols: $\Phi_{u'}$ (— straight trailing edge, ● serrated sawtooth trailing edge); $\Phi_{v'}$ (— straight trailing edge, ● serrated sawtooth trailing edge). (For interpretation of the references to color in this figure legend, the reader is referred to the web version of this article.)

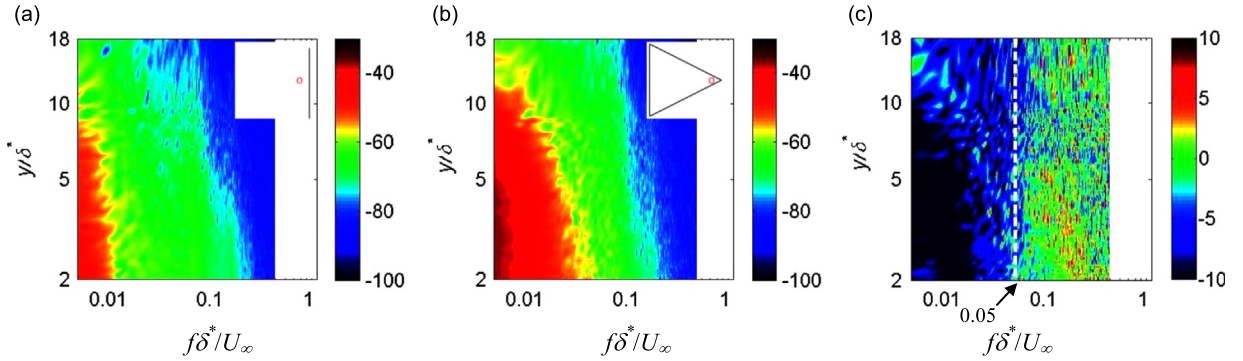

Fig. 12. Comparison of velocity–wall pressure cross spectral densities at location E1 for (a) straight trailing edge ($\Phi^o_{(u'v'),p'}$), (b) serrated sawtooth trailing edge ($\Phi^*_{(u'v'),p'}$), and (c) $\Delta\Phi=[\Phi^o_{(u'v'),p'}-\Phi^*_{(u'v'),p'}]$.

the level of $\Phi_{(u'v'),p'}$ is higher than the straight edge counterpart in Fig. 12a, especially at low frequencies. A new quantity $\Delta\Phi=[\Phi_{(u'v'),p'(\text{straight})}-\Phi_{(u'v'),p'(\text{sawtooth})}]$ is also introduced. A negative $\Delta\Phi$ therefore implies that the level of contribution $(u'v')$ in the boundary layer to the wall pressure generation by a serrated sawtooth trailing edge is greater than for the straight trailing edge, and vice versa. In Fig. 12c for the $\Delta\Phi$ contour map, a distinct division line at $f\delta^*/U_\infty \approx 0.05$ can be observed. This value is similar to the Strouhal number pertaining to the spectral hump peaks in Fig. 11c which were determined by the fluctuating velocity power spectral density in the boundary layer. Therefore it is clear that below a Strouhal number of 0.05, the $(u'v')$ fluctuating term across the boundary layer contributes significantly to the wall pressure generation.

In order to further study the net level of cross spectral density, another quantity $\Delta\zeta$, which is related to $\Delta\Phi$, is introduced

$$\Delta\zeta(x,y,z)=10\log_{10}\left[\frac{\int\left(u'v'\cdot\overline{P}'^2\right)_{\text{straight}}(x,y,z,f)\mathrm{d}f}{\int\left(u'v'\cdot\overline{P}'^2\right)_{\text{sawtooth}}(x,y,z,f)\mathrm{d}f}\right]. \tag{4}$$

A considerable deficit of about −10 dB in $\Delta\zeta$ is shown in Fig. 13 (demonstrated by the + symbol), thereby supporting the earlier notion that the high level of wall pressure fluctuation at the sawtooth tip is mainly contributed by the dynamics of the boundary layer instead of the acoustical back scattering.

It should be noted that the unsteady wall pressure *PSD* level $\Phi_{p'}$ near the sawtooth tip for a serrated sawtooth trailing edge is substantially larger than for the straight trailing edge. Hence, there is a possibility that the results presented in Fig. 12b might have been biased towards producing a larger level of $\Phi_{(u'v'),p'}$ for the serrated sawtooth trailing edge. To investigate this issue further, the wall pressure raw data is normalized with the root-mean-square pressure, P_{rms}, and then a "normalized" power spectral density (or power cross spectral density) can be calculated. Because a clear dividing line for the Strouhal number has been demonstrated earlier in the $\Delta\Phi$ contour, this analysis will only focus on $f\delta^*/U_\infty \leq 0.05$. The power spectral densities of the normalized wall pressure $\Phi_{(p'/\text{Prms})}$ for both the straight and serrated sawtooth trailing edges are plotted in Fig. 14a. The figure shows that the two cases collapse well. The cross spectral density between the product of the two-component velocity fluctuations $(u'v')$ within a boundary layer and the now normalized wall pressure is denoted by $\Phi_{(u'v'),(p'/\text{Prms})}$. Subsequently, $\Phi_{(u'v'),(p'/\text{Prms})}$ can be calculated for both the straight and serrated sawtooth trailing edges, before a new $\Delta\Phi$ is obtained. As shown in Fig. 14b, the new $\Delta\Phi$ contour still demonstrates a higher level of $\Phi_{(u'v'),(p'/\text{Prms})}$

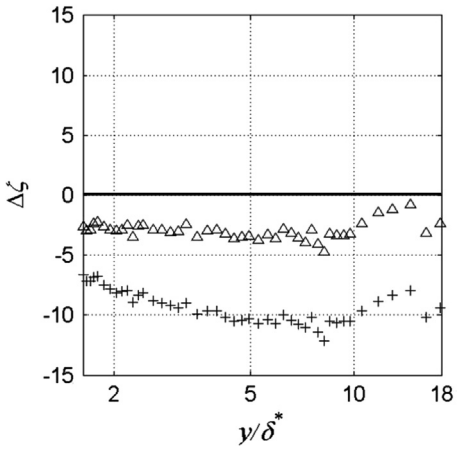

Fig. 13. Distribution of $\Delta\zeta$ across the boundary layer at location E1, which represents cross spectral between the $(u'v')$ and the absolute pressure fluctuations p' (+), or the normalized pressure fluctuations p'/p_{rms} (Δ).

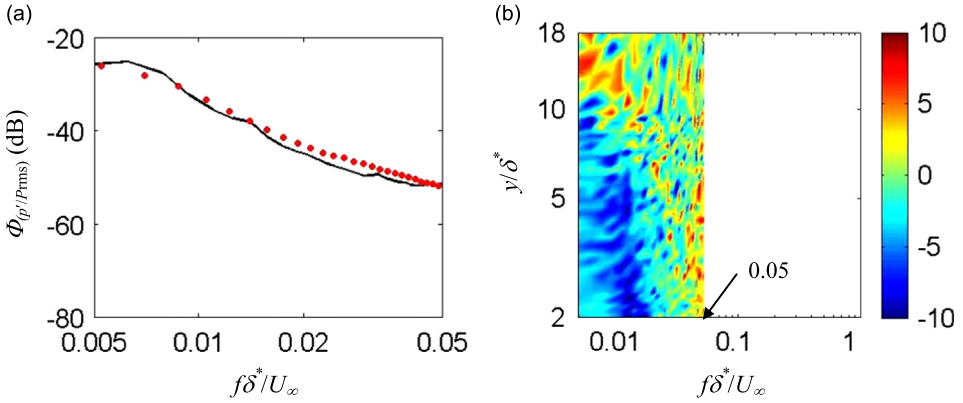

Fig. 14. (a) Power spectral densities at location E1 for the straight trailing edge $\Phi^{o}_{(p'/Prms)}$ (—) and serrated sawtooth trailing edge $\Phi^{*}_{(p'/Prms)}$ (●) and (b) $\Delta\Phi = [\Phi^{o}_{(u'v').(p'/Prms)} - \Phi^{*}_{(u'v').(p'/Prms)}]$. (For interpretation of the references to color in this figure legend, the reader is referred to the web version of this article.)

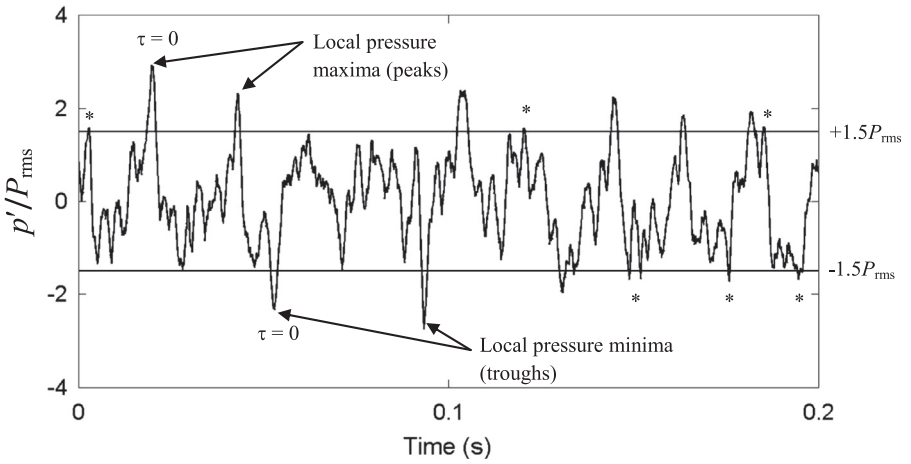

Fig. 15. Surface pressure signals and the two threshold lines ($\pm 1.5P_{\mathrm{rms}}$) selected to calculate the conditionally-averaged velocity associated with the pressure peaks and pressure troughs. The minor pressure peaks and pressure troughs just passing the thresholds, which are marked as * in the figure, are not included in the ensemble.

for a serrated sawtooth trailing edge. The corresponding $\Delta\zeta$, which is shown in Fig. 13 by the symbol "Δ", achieves an average level of -3.5 dB.

6.2. Conditional-averaged velocity perturbations, rms velocity fluctuations and Reynolds shear stresses

The basis of the conditional-averaging technique is similar to Sagrado [26] and Daoud [27]. In this method the positive wall pressure peaks and negative wall pressure troughs in the time domain can be used as references for the ensemble averaging of the mean and fluctuating velocity signals. To illustrate the technique, an example of the wall pressure signal in the time domain is plotted in Fig. 15. First, arbitrarily thresholds of $\pm 1.5P_{\mathrm{rms}}$ were selected to identify the blocks of time relative to the dominant positive and negative wall pressure oscillations, where P_{rms} is the rms value of a wall pressure data set. The pressure peak (or trough) at each identified time block is assigned to $\tau=0$. Therefore $\tau<0$ and $\tau>0$ represent times in advance and time delay, respectively, from the occurrence of the pressure peak/trough. Once the times at which the pressure peaks/troughs have been identified for the entire pressure signals, the velocity signals can be ensemble-averaged accordingly. Approximately 1400 ensembles were available to calculate the conditional-averaged velocities at each measurement point. Using this simple method, some coherent structures can be identified from the turbulent boundary layer. A point to note is that there is a slight phase difference between the wall pressure and the X-wire signals. However, this has no influence on the accuracy of the current ensemble analysis because the structure is only slightly shifted with reference to the $\tau=0$.

The identification of the coherent structures is taken on the basis of triple decomposition of the velocity field [28,29]:

$$U_k(x,y,z,t)=U_{m,k}(x,y,z)+u_{c,k}(x,y,z,t)+u_{r,k}(x,y,z,t). \tag{5}$$

The index k represents the velocity components in either the x or y direction. U is the instantaneous velocity, U_m is the mean velocity, u_c is the coherent velocity and u_r is the incoherent velocity fluctuations. The coherent velocity u_c can be calculated by taking the difference between the ensemble-averaged total velocity and time-averaged mean velocity, i.e. $u_c=\langle U\rangle-U_m$. Note that the angular brackets represent ensemble-averaging, which are based on the positive wall pressure $\langle+P\rangle$ and negative wall pressure $\langle-P\rangle$ that exceed the threshold values of $\pm 1.5P_{\mathrm{rms}}$. The velocity perturbation, which measures the momentum excess or deficit caused by a coherent structure, is obtained by scaling the coherent velocity with the local freestream velocity U_∞. The temporal variations of the velocity perturbations, $\tilde{U}$and $\tilde{V}$, are therefore

$$\tilde{U}(x,y,z,\tau)=\frac{<U(x,y,z,\tau)>-U_m(x,y,z)}{U_\infty(x,z)}, \tag{6a}$$

$$\tilde{V}(x,y,z,\tau)=\frac{<V(x,y,z,\tau)>-V_m(x,y,z)}{U_\infty(x,z)}. \tag{6b}$$

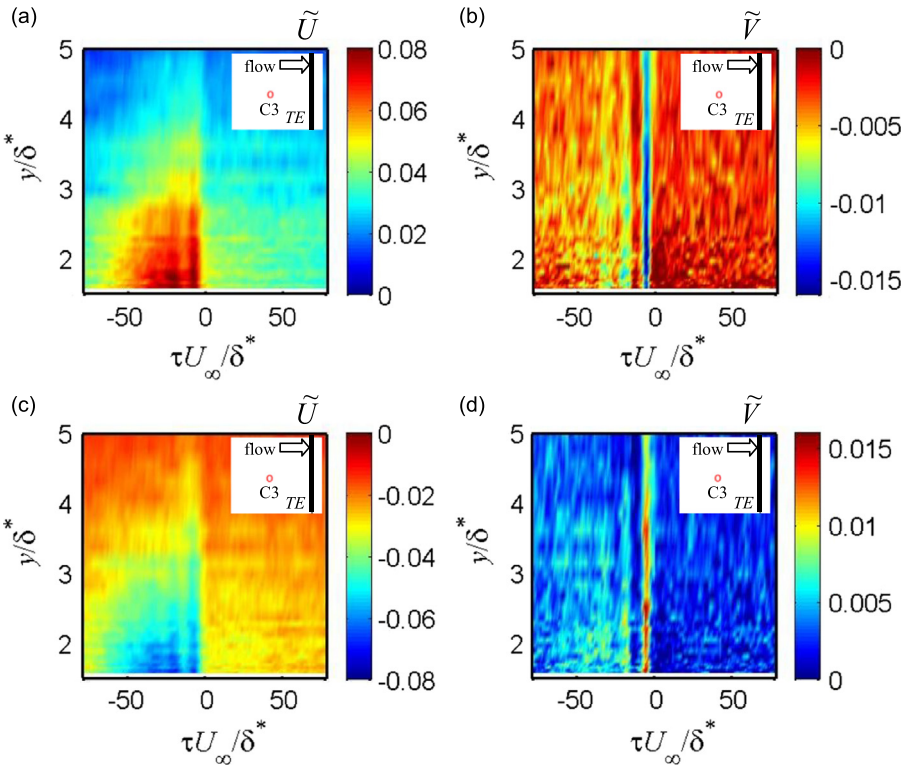

Fig. 16. Contours of $\tilde{U}$ and $\tilde{V}$ for (a and b) $\langle+P\rangle$ surface pressure, and (c and d) $\langle-P\rangle$ surface pressure. The measurement location is at C3 for the straight trailing edge.

Similarly, if the temporal variations of the rms fluctuations of U and V at each measurement point are represented by u_{rms} and v_{rms} respectively, they can be calculated as

$$u_{\mathrm{rms}}(x,y,z,\tau)=\sqrt{\frac{\sum_{i=1}^{N}\left[U(x,y,z,\tau)-\langle U(x,y,z,\tau)\rangle\right]^2}{N}}, \tag{7a}$$

$$v_{\mathrm{rms}}(x,y,z,\tau)=\sqrt{\frac{\sum_{i=1}^{N}\left[V(x,y,z,\tau)-\langle V(x,y,z,\tau)\rangle\right]^2}{N}}, \tag{7b}$$

where N is the number of realizations. Finally, the temporal variations of the Reynolds shear stress $\langle u'v'\rangle$ can be calculated from the following equation:

$$\langle u'v'\rangle(x,y,z,\tau)=\frac{\sum_{i=1}^{N}\left[U(x,y,z,\tau)-\langle U(x,y,z,\tau)\rangle\right]\left[V(x,y,z,\tau)-\langle V(x,y,z,\tau)\rangle\right]}{N}. \tag{8}$$

Note that the above conditional averaging technique can only identify time-averaged structures associated with the surface pressure fluctuations. The analysis cannot provide information about the mechanisms responsible for the wall pressure generation from the velocity field in the boundary layer, which normally requires stochastic estimation technique [30,31].

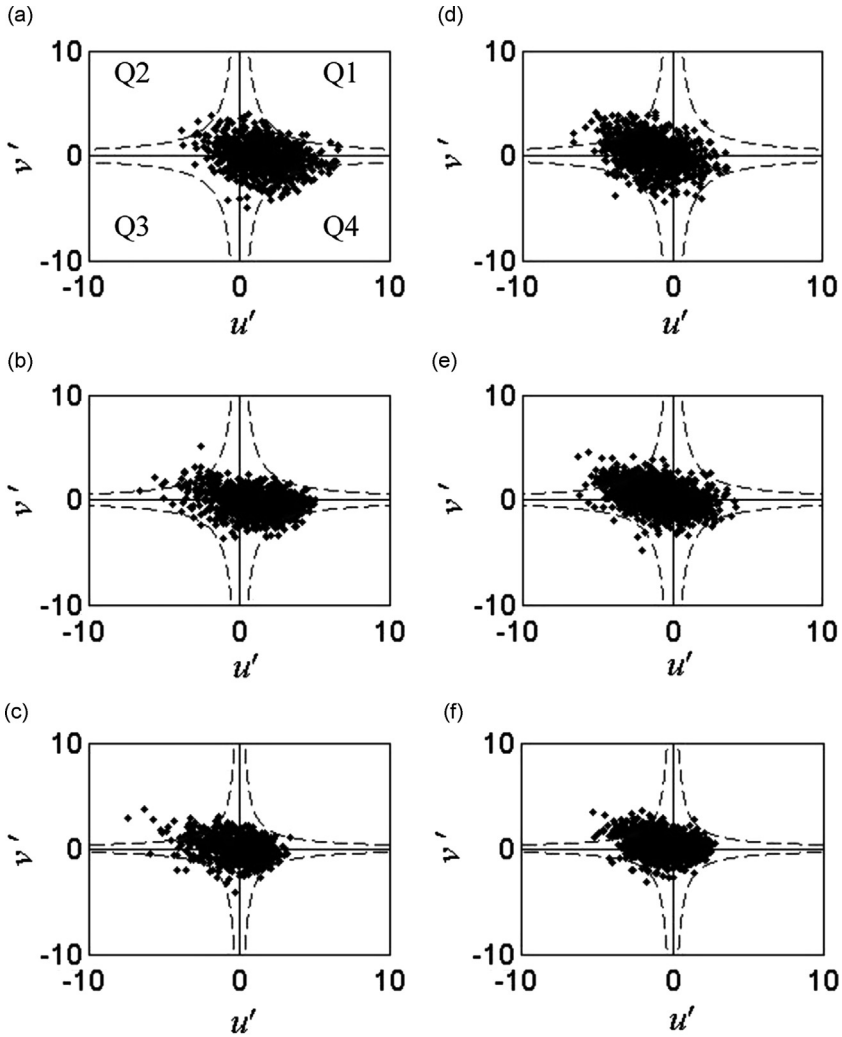

Fig. 17. Distributions of instantaneous u' and v' that correspond to (a, b, and c) pressure peaks at $y/\delta^*=1.4$, 3.2 and 5.7, respectively; and (d, e, and f) pressure troughs at $y/\delta^*=1.4$, 3.2 and 5.7, respectively. The measurement location is at C3 for the straight trailing edge. The broken lines (– – –) represent the hyperbola $|u'v'|=6\times-\overline{u'v'}$.

The main purpose in this paper is to compare the changes in the temporal variations in velocity perturbation, rms velocity fluctuation and Reynolds shear stress when the structures develop on a straight trailing edge and a sawtooth trailing edge.

6.2.1. General characteristic of the coherent structures on a two-dimensional turbulent boundary layer

First, it will be useful to discuss the general characteristics of two-dimensional turbulent boundary layer. For this reason the results presented in this section are only related to the unserrated, straight trailing edge. Contour maps of $\tilde{U}$ and $\tilde{V}$ for $\langle +P\rangle$ and $\langle -P\rangle$ pertaining to location C3 are shown in Fig. 16. Note that the axes in the figures are scaled with the local boundary layer displacement thickness (δ^*) and freestream velocity (U_∞). By examining the $\tilde{U}$ contours for $\langle +P\rangle$ in Fig. 16a, $\tilde{U}$ is mainly positive at $\tau U_\infty/\delta^* < 0$ (prior the occurrence of the pressure peak) and a coherent structure is discernible. However, the $\tilde{V}$ velocity perturbations near the pressure peak in Fig. 16b are found to be mostly negative in sign, which contradict their $\tilde{U}$ perturbation counterpart. The high momentum excess at $\tau U_\infty/\delta^* < 0$ for the $\tilde{U}$ perturbation contour, i.e. ($\tilde{U} > 0$), could be analogous to an instantaneous fluctuating velocity for which $u' > 0$ (this correlation will be examined later). The corresponding $\tilde{V}$ perturbation of $\tilde{V} < 0$ should then denote negative instantaneous fluctuating velocity $v' < 0$. This combination therefore suggests that a Q4-quadrant event is dominant for the case of $< +P >$. Physically, a high-speed flow is sweeping towards the near wall region (or to the back of hairpin vortices) following a bursting event which is associated with the organized structures in a turbulent boundary layer [32–34].

As shown in Fig. 16c, coherent structure is also discernible for the $\langle -P\rangle$ case although it is now characterized by negative values of $\tilde{U}$ at $\tau U_\infty/\delta^* < 0$ (prior the occurrence of the pressure trough). The $\tilde{V}$ velocity perturbation in Fig. 16d is mostly positive in sign against its $\tilde{U}$ perturbation counterpart. Similarly, the combination of ($\tilde{U} < 0$, $u' < 0$) and ($\tilde{V} > 0$, $v' > 0$) suggests the presence of a Q2-quadrant event. Physically, low-momentum fluid is ejected between the counter rotating legs

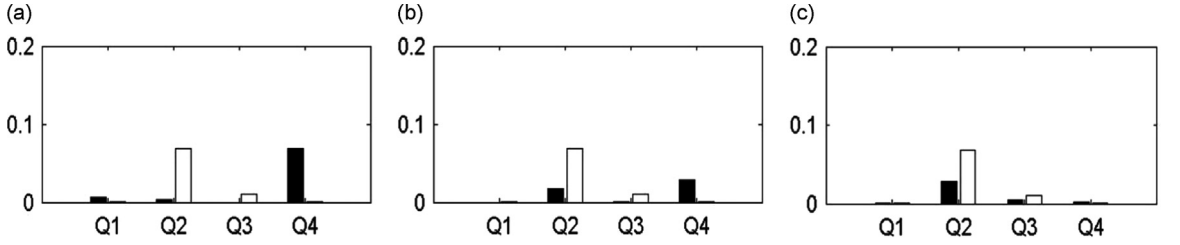

Fig. 18. Fractions of the "intense" $u'v'$ events that correspond to the pressure peaks (black bars) and the pressure troughs (white bars) at different quadrants (Q1, Q2, Q3 and Q4) for (a) $y/\delta^* = 1.4$, (b) $y/\delta^* = 3.2$, and (c) $y/\delta^* = 5.7$. The measurement location is at C3 for the straight trailing edge.

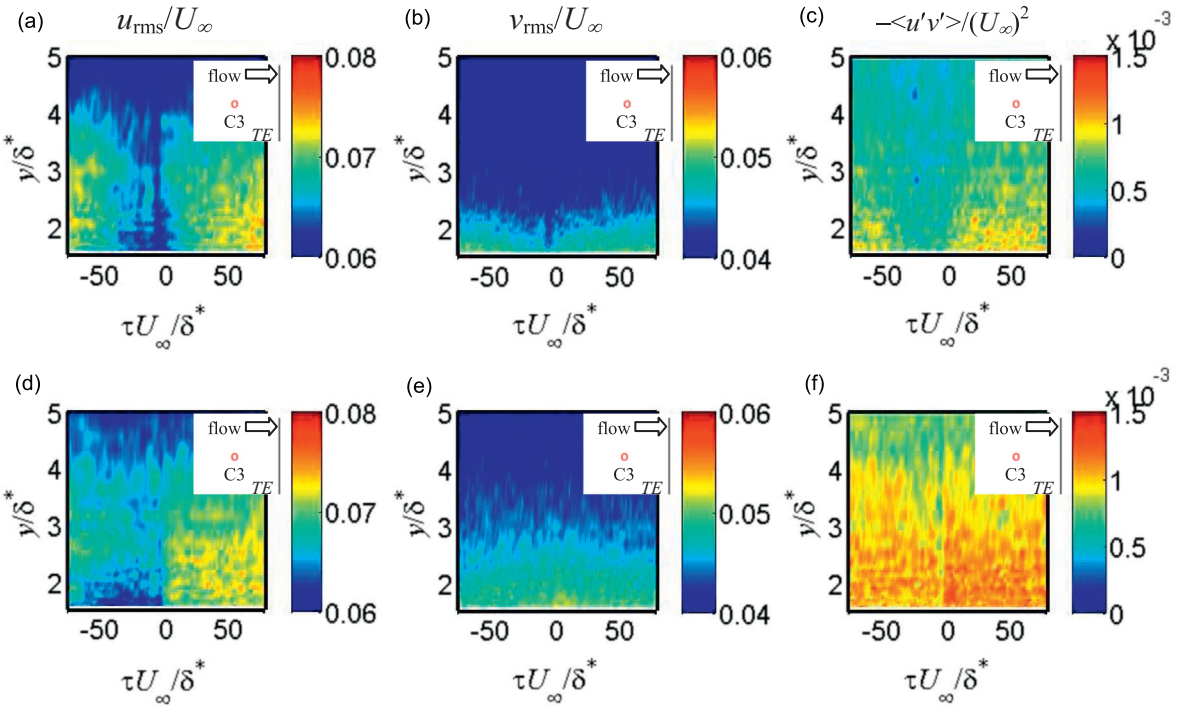

Fig. 19. Contours of u_{rms}/U_∞, v_{rms}/U_∞ and $-\langle u'v'\rangle/(U_\infty)^2$ for (a, b, and c) $\langle +P\rangle$ surface pressure, and (d, e, and f) $\langle -P\rangle$ surface pressure. The measurement location is at C3 for the straight trailing edge.

of the hairpin vortices. The lifted low-momentum fluids, which are long and persistent in the higher velocity buffer layer, will eventually oscillate and break up. This cyclic event is commonly recognized as the main mechanisms for the generation of turbulent energy [32–34].

In Reynolds decomposition the instantaneous velocity fluctuation u' is the difference between the instantaneous velocity U and time-mean velocity U_m. The ensemble-average of the velocity fluctuation, which will produce non-zero values, is therefore related to the coherent velocity, i.e. $\langle u' \rangle = \langle U - U_m \rangle = u_c$. This relationship allows the ensemble-averaged velocity perturbations to be used to describe the quadrant events of a turbulent boundary layer which we did in the previous paragraphs. To illustrate this, plots of instantaneous $u'$and v' distribution at $y/\delta^* = 1.4$, 3.2 and 5.7 for the $\langle +P \rangle$ and $\langle -P \rangle$ cases are shown in Fig. 17. The figure shows the contribution to the Reynolds shear stress from each quadrant as a function of y/δ^*. There are approximately 1400 data points (representing all ensembles) in each plot, which displays a collection of u' and v' data points that correspond to $\tau U_\infty/\delta^*$ occurring at either the pressure peaks (for the $\langle +P \rangle$ case) or pressure troughs (for the $\langle -P \rangle$ case). Phase difference between the microphone and X-wire signals was taken into consideration. Essentially, the unsteady wall pressure signals have been used to identify the quadrant events in the total turbulence production. In the relatively near wall region at $y/\delta^* = 1.4$ and 3.2, as shown in Fig. 17a and b respectively, most of the $u'$and v' data points for the pressure peaks can be found in the Q4-quadrant. However, for the pressure troughs the $u'$and v' data points concentrate in the Q2-quadrant (Fig. 17d and e). At a slightly higher location at $y/\delta^* = 5.7$, the $u'$and v' data points associated with both the pressure peaks and troughs seem to be slightly concentrated within the Q2-quadrant, as shown in Fig. 17c and f respectively. In general, however, they are more evenly distributed among the other quadrants at this particular wall normal position.

Each plot in Fig. 17 also contains hyperbolas corresponding to $|u'v'| = 6 \times -\overline{u'v'}$, which serve to identify the instantaneous Reynolds shear stresses $u'v'$ that are larger than six times the mean Reynolds shear stress (symbols outside the hyperbolas).

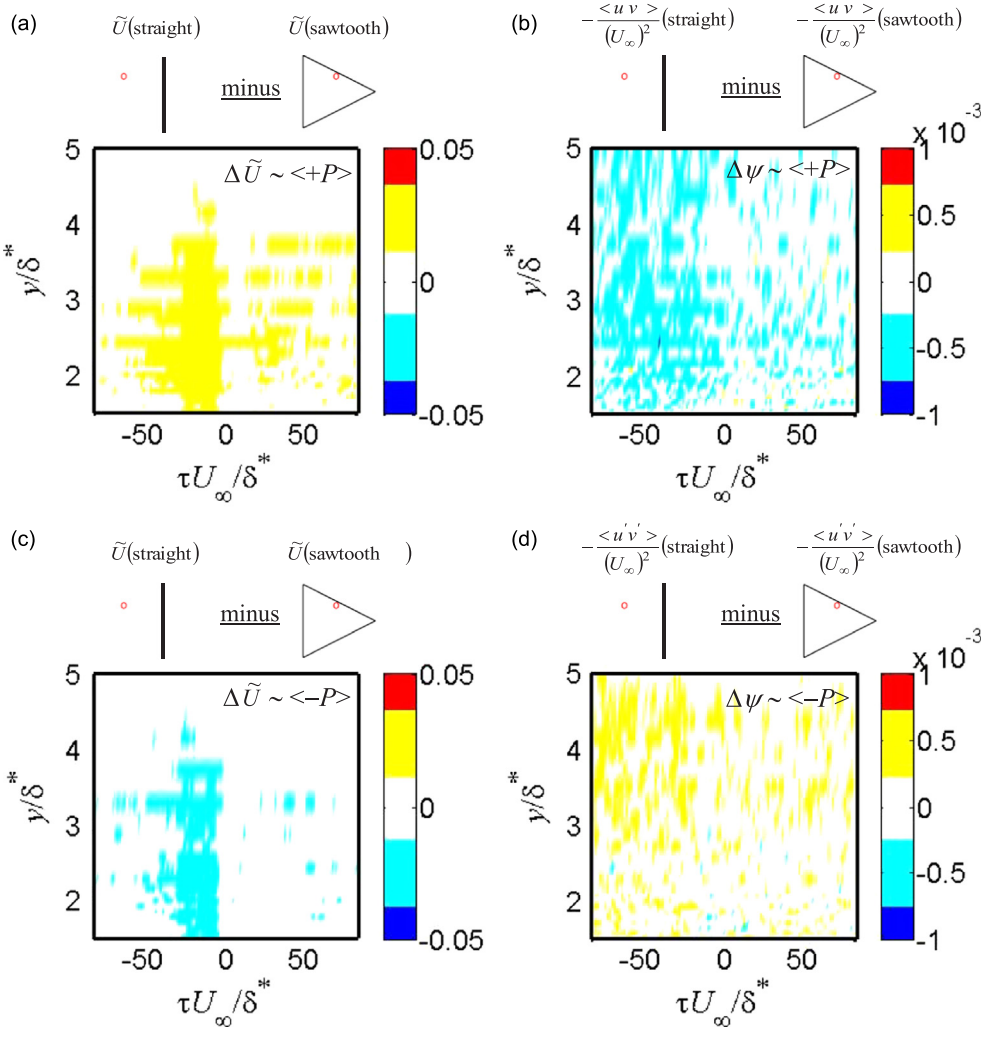

Fig. 20. Contours of $\Delta\tilde{U}$ and $\Delta\psi$ for (a and b) $\langle +P \rangle$ surface pressure, and (c and d) $\langle -P \rangle$ surface pressure. The measurement location is at C1 for both of the straight and serrated sawtooth trailing edge.

Note that the constant value of 6 for the above equation is chosen arbitrarily to distinguish the intense $u'v'$ events from others. The bar chart in Fig. 18 represents the fraction of the intense $u'v'$ events of each quadrant to the total number of ensembles for the positive pressure peaks and negative pressure troughs. The figure contains results for the straight trailing edge at location C3. They clearly demonstrate that the intense sweep event is dominant at the near wall region but becoming weaker at further height. However, the intense ejection event can be found up to at least $y/\delta^*=5.7$. Note that a similar analysis of the intense $u'v'$ events at the same location C3 for a sawtooth serrated trailing edge also produces the same trends.

The coherent motion of the substructures in a turbulent boundary layer with respect to the $\langle +P\rangle$ and $\langle -P\rangle$ cases can also be described by the velocity fluctuations $u_{\rm rms}/U_\infty$, $v_{\rm rms}/U_\infty$ and Reynolds shear stresses $-\langle u'v'\rangle/(U_\infty)^2$ in Fig. 19. For the $\langle +P\rangle$ case in Fig. 19a, the wall inward sweeping motion is accompanied by particularly low values of $u_{\rm rms}/U_\infty$ between $-40<\tau U_\infty/\delta^*<20$, as well as predominantly low values of $v_{\rm rms}/U_\infty$ throughout the time of flight in Fig. 19b. The low level of velocity fluctuations in Fig. 19a and b and the high-momentum fluids in Fig. 16a demonstrate that the $\langle +P\rangle$ case is associated with a low turbulence production, which is further manifested in the Reynolds shear stress $-\langle u'v'\rangle/(U_\infty)^2$ contour in Fig. 19c. On the other hand, the ejection event produces much higher Reynolds shear stress levels in the $\langle -P\rangle$ case (see Fig. 19f). A similar observation can also be found in the $v_{\rm rms}/U_\infty$ levels in Fig. 19e., and to a lesser extent in the U_{rms}/U_∞ contour in Fig. 19d.

As shown by Vathylakis and Chong [21], the velocity perturbations, *rms* velocity fluctuations and Reynolds shear stresses at location C3 are quantitatively very similar between the straight trailing edge and the serrated sawtooth trailing edge. In other words, the sawtooth does not affect the momentum transfers and turbulence transports at location outside the sawtooth side edge and sawtooth tip. This is consistent with the surface temperature and unsteady wall pressure *PSD* contour maps presented earlier.

6.2.2. *Development of the coherent structures near the sawtooth side edges*

This section focuses on the momentum transfers and turbulence transports at a location close to the side edge of a serrated sawtooth trailing edge (i.e. location C1). Comparison is made against the straight trailing edge at the same location. For brevity, only the velocity perturbations $\tilde{U}$ and Reynolds shear stresses $-\langle u'v'\rangle/(U_\infty)^2$ are discussed in this section. For ease of comparison, the results are presented using the notations

$$\Delta\tilde{U}=\tilde{U}_{\rm straight}-\tilde{U}_{\rm sawtooth} \tag{9}$$

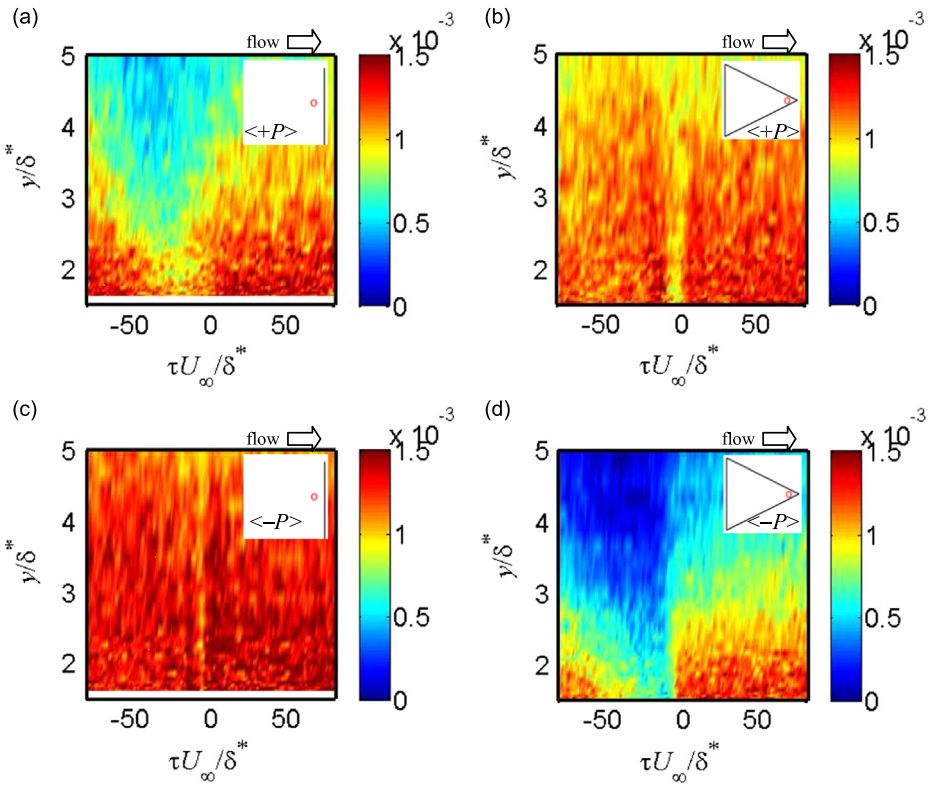

Fig. 21. Contours of $-\langle u'v'\rangle/(U_\infty)^2$ for (a and b) $\langle +P\rangle$ surface pressure, and (c and d) $\langle -P\rangle$ surface pressure. The measurement location is at E1 for both of the straight trailing edge and serrated sawtooth trailing edge.

$$\Delta\psi = -\langle u'v'\rangle/(U_\infty)^2_{\text{straight}} + \langle u'v'\rangle/(U_\infty)^2_{\text{sawtooth}}. \tag{10}$$

As shown in Fig. 20a, the predominantly positive $\Delta\tilde{U}$ demonstrates that the high-momentum wall sweeping event at $\tau U_\infty/\delta^* < 0$, which is associated with $\langle +P\rangle$, becomes less significant near the sawtooth side edge for the serrated trailing edge. Interestingly, in Fig. 20c, the predominantly negative $\Delta\tilde{U}$ during the $\langle -P\rangle$ cycle demonstrates that the low-momentum ejection event near the sawtooth side edge for the serrated trailing edge is also less significant. The above momentum transfers ($\Delta\tilde{U}$) of the substructures near a sawtooth side edge are also manifested in the turbulence production observed in the $\Delta\psi$ contours. As shown in Fig. 20b, a higher Reynolds shear stress level is generally produced during the $\langle +P\rangle$ cycle near the sawtooth side edge of the serrated trailing edge because of the predominantly negative values of $\Delta\psi$. This implies that the becalmed effect of the wall sweeping of high-momentum fluids is less significant near the sawtooth side edge. On the other hand, because of the weakened ejection and bursting of low-momentum fluids near the sawtooth side edge of the serrated trailing edge during the $\langle -P\rangle$ cycle, Fig. 20d shows a predominantly positive value of $\Delta\psi$. This means that the serrated trailing edge produces a Reynolds shear stress level which is lower than the straight edge counterpart. As a result, the mechanism of turbulence production based on the sweep-and-eject model near the side edge of the serrated sawtooth trailing edge is quite different from the turbulence production mechanism on the straight trailing edge.

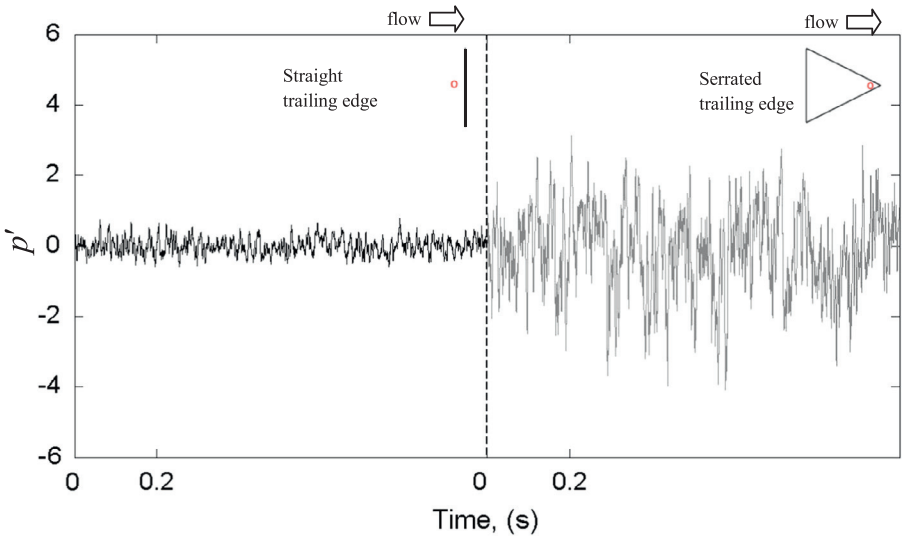

Fig. 22. Comparison of the surface pressure signal amplitudes measured at location E1 between the straight trailing edge and serrated sawtooth trailing edge. Note that both the pressure signals were measured by the same microphone and amplifier.

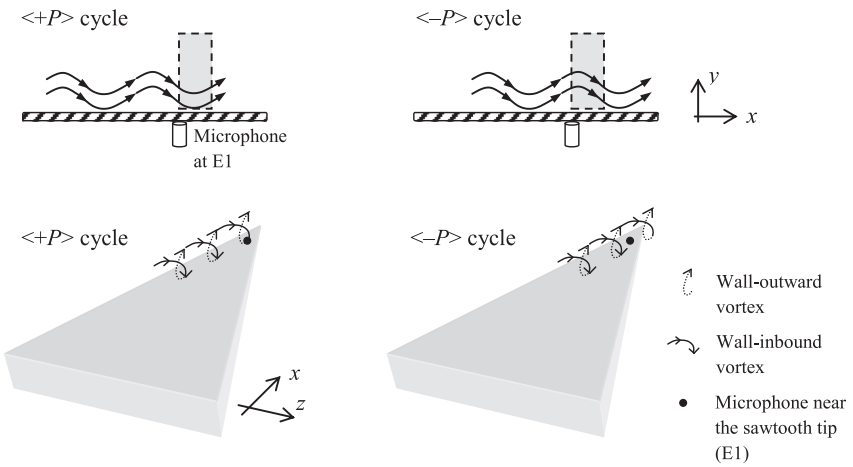

Fig. 23. Schematics to illustrate the propagations of the pressure-driven vortical structures near the sawtooth side edge towards the tip for the $\langle +P\rangle$ and $\langle -P\rangle$ cycles. Top figures: *side view*; bottom figures: *isometric view*. Drawings are not to scale.

Despite the change in flow dynamics near the sawtooth side edge of the serrated trailing edge, the time-averaged Reynolds shear stresses $-\overline{u'v'}/U_\infty^2$ profiles for the straight and serrated sawtooth trailing edges are actually quite similar (see Fig. 10b for location C1). Normally, the anti-correlation of the sweeps and ejections gives rise to Reynolds shear stress. The results presented in Fig. 20 are therefore mainly due to the simultaneously-weakened sweep and ejection motions near the sawtooth side edge of the serrated trailing edge. In this scenario, the sweeps will produce higher than usual Reynolds shear stress levels while the ejections will produce the opposite, resulting in an overall balanced level as manifested in the time-averaged Reynolds shear stress.

The results in this section suggest that the turbulent boundary layer near the side edge of a serrated sawtooth trailing edge has been influenced by the side edge vortical structure. Further investigation is conducted for the flow dynamics near the sawtooth tip, which will be discussed in the next section.

6.2.3. *Development of the coherent structures near the sawtooth tip*

Fig. 21 presents the contour maps of $-\langle u'v'\rangle/(U_\infty)^2$ at E1, which is the location close to the sawtooth tip. The most striking feature in the figure is that the Reynolds shear stresses are anti-correlated between the straight and serrated sawtooth trailing edges with respect to the $\langle +P\rangle$ and $\langle -P\rangle$ cycles. The becalmed effect of the wall sweeping motion during the $\langle +P\rangle$ cycle, as demonstrated in the straight trailing edge in Fig. 21a, is totally absence for the serrated sawtooth trailing edge in Fig. 21b. However, a seemingly very high-momentum wall sweeping motion is present for the serrated sawtooth trailing edge during the $\langle -P\rangle$ cycle in Fig. 21d. This contradicts the straight trailing edge in which the boundary layer is mostly characterized by high turbulence production during this particular cycle (see Fig. 21c).

Previously, we have demonstrated that the unsteady wall pressure *PSD* level and the wall heat transfer will increase significantly near the sawtooth tip. This can be further illustrated in Fig. 22 by the comparison of wall pressure time-signals between the straight and serrated sawtooth trailing edges at location E1. Therefore, the use of wall pressure peaks and troughs as the reference signals at location E1 for the serrated sawtooth trailing edge is likely to contain certain elements of vortical flow in the ensemble-averaged momentum/turbulence quantities. The Reynolds shear stress contours in Fig. 21b and d should then reflect the turbulent boundary layer flow subjected to interaction with the side edge vortical flow. As a result, direct comparison of the ensemble-averaged Reynolds shear stress contours between the straight and serrated sawtooth trailing edges may not be straightforward.

The mechanism which is responsible for producing the opposite temporal pattern of the Reynolds shear stress in Fig. 21 could be explained by the idealized schematics in Fig. 23, which depict the propagation of the pressure-driven disturbances

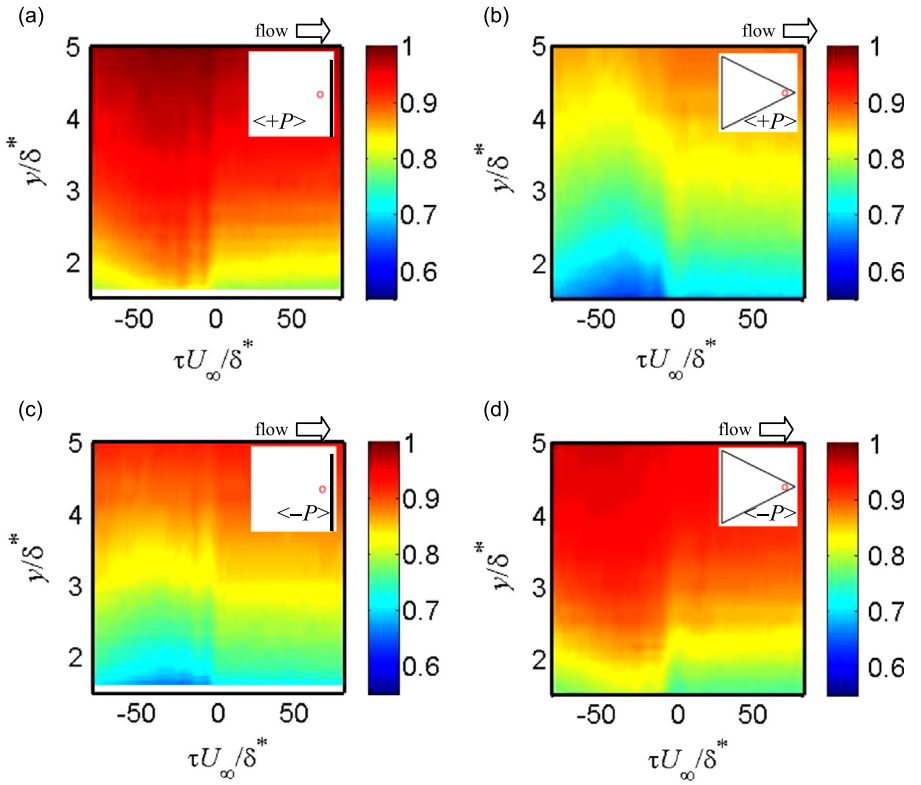

Fig. 24. Contours of $\langle U\rangle/U_\infty$ for (a and b) $\langle +P\rangle$ surface pressure, and (c and d) $\langle -P\rangle$ surface pressure. The measurement location is at E1 for both of the straight trailing edge and serrated sawtooth trailing edge.

in a convective vortical pattern along the oblique side edge of a sawtooth. This type of flow interaction has two main characteristics which should be a priori:

(1) As demonstrated in Fig. 22, the level of pressure fluctuations produced by the vortical flow is significantly larger than the level of pressure fluctuations produced by the viscous effect in the turbulent boundary layer.
(2) The sweep and ejection of the turbulent boundary layer will be affected in accordance with the phase of the convecting vortical structure.

The following discussion is only related to the serrated sawtooth trailing edge. Considering first the $\langle +P \rangle$ case on the left-hand-side of Fig. 23, the wall-inward motion of the arriving vortices will induce large positive pressure fluctuations across the boundary layer. Based on the characteristic (1) described above, the positive pressure fluctuations could already be captured by the surface microphone at some distances downstream. During the same phase when the microphone is measuring the positive pressure fluctuation, the finite area above it (indicated by the shaded box) will be subjected to an upward motion of the vortices where the low-momentum fluid is entrained from the wall. To demonstrate this, ensemble-averaged velocity $\langle U \rangle / U_\infty$ for the straight and serrated sawtooth trailing edges during the $\langle +P \rangle$ cycle are compared in Fig. 24a and b, respectively. It can be seen that lower level of $\langle U \rangle / U_\infty$ is produced in the boundary layer for the serrated sawtooth trailing edge prior to the arrival of the pressure peak. Because the shaded box in Fig. 23 coincides with the X-wire probe, a predominantly upward low-momentum fluid, with a high value of Reynolds shear stress in the boundary layer as manifested in Fig. 21b, will be measured.

After one half of a period, as demonstrated at the right-hand-side of Fig. 23, the vortices upstream of the surface microphone sensor will be predominantly subjected to wall-outward motion because of the convective nature of the vortices. The surface microphone will therefore measure negative wall pressure fluctuations $\langle -P \rangle$ during this phase. Using the same principle described in the previous paragraph, the vortices will induce high momentum fluids sweeping towards the wall within the shaded box. This is also manifested in the $\langle U \rangle / U_\infty$ contours for the straight and serrated sawtooth trailing edges in Fig. 24c and d, respectively. The mechanism underpinning the significantly reduced Reynolds shear stress level in the boundary layer during the $\langle -P \rangle$ cycle, as shown in Fig. 21d, is thus provided.

In summary, due to the vortical structure near the tip of a serrated sawtooth trailing edge, the ensemble-averaged velocities measured by the X-wire within the boundary layer will be out of phase with the wall pressure signals.

7. Discussion

In the liquid crystal experiments for both wide-angle and narrow-angle sawtooth, the sawtooth's oblique side edges and tips are shown to exhibit a lower temperature than the straight trailing edge, whilst the temperature difference at other places remains unchanged. A lower surface temperature is caused by higher heat transfer rate, which is associated with a higher level of turbulence.

Wall pressure *PSD* at 34 locations is mapped on a complete sawtooth surface of a serrated trailing edge. An equivalent distribution of the wall pressure *PSD* is also obtained for the straight trailing edge. The frequency range over which noise reduction occurs is found to feature the co-existence of strong wall pressure fluctuations near the sawtooth side edges and the sawtooth tips. The wall pressure spectral energy, which is obtained from the integration of the wall pressure *PSD* with frequency, also resembles strong fluctuations at locations near the sawtooth oblique side edge and sawtooth tip. The contribution of the acoustical back-scattered pressure to the wall pressure *PSD* and spectral energy, if any, has been proven to be negligible in the current case.

Extensive streamwise and spanwise coherence measurements were performed. Generally, it was found that the convective velocities of the turbulent eddies in the streamwise direction (and without the spanwise spacing) are very similar for both the straight and sawtooth serrated trailing edges. On the other hand, when the microphone pairs are separated in the spanwise direction (and without the streamwise spacing), some noticeable differences are found

(1) The measured spanwise wall pressure coherence functions for the straight trailing edge follow the predicted curves by Brooks and Hodgson [25]. The measured phase differences in the spanwise direction are almost zero, which suggest that there is no convection velocity of eddies in this direction.
(2) However, for the *serrated sawtooth trailing edge*, the measured spanwise coherence functions at regions close to the sawtooth oblique side edge and tip are slightly higher than the straight edge counterpart.

Amiet [12] stipulates that $S_{pp}(\omega) \propto L(\omega) I_y(\omega) S_{qq}(\omega)$. The variations of the spanwise coherence (which relates to the spanwise correlation length I_y) are generally not too significant between a straight and a serrated sawtooth trailing edge. However, the overall S_{qq} (and heat transfer) in a serrated sawtooth trailing edge is found to be higher than the straight trailing edge counterpart. This result would have contradicted the Amiet's model and the prediction of noise reduction by a serrated sawtooth trailing edge. In order to explain this the investigation then focuses on the flow structures developed on a serrated sawtooth surface.

Table 1
Convection velocities determined by the phase spectral.

Microphone pair	Flow →	Δx (mm)	Δz (mm)	U_c for straight trailing edge (m s^{-1})	U_c for serrated trailing edge (m s^{-1})	ΔU_c (%)
B4–C3		4	0	19.6	18.6	5.1
B2–C1		4	0	19.5	19.1	2.1
B1–C1		4	2	24.5	12.9	**47.3**
C1–D1		4	2	24.2	10.2	**57.9**
D1–E1		4	2	23.5	13.2	**43.8**
B2–C2		4	2	24.3	24.7	−1.6
C2–D2		4	2	22.7	24.4	−7.5

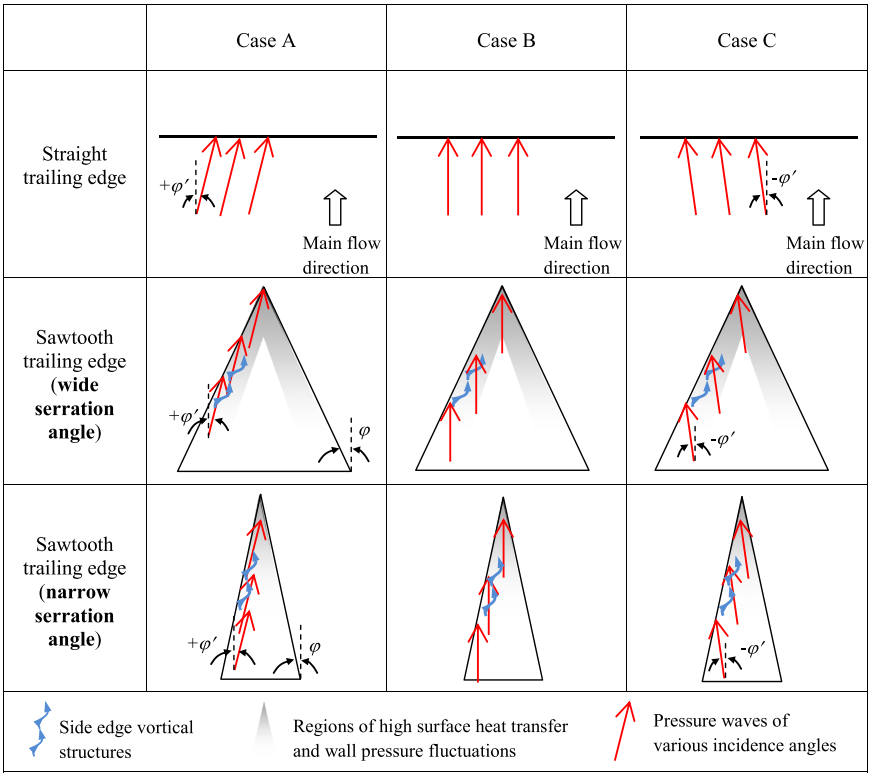

Fig. 25. Schematics to illustrate the propagations of the boundary layer pressure waves of various incidence angles to the different trailing edges. Note that both the wide and narrow serration angles have the same 2*h*. Drawings are not to scale.

Boundary layer measurements were performed at several locations on the straight and serrated sawtooth trailing edges using an X-wire. The time-averaged Reynolds shear stress profiles are generally similar when comparing the straight and serrated sawtooth trailing edges, except at the sawtooth tip where an increase of up to 8% at the near wall region has been

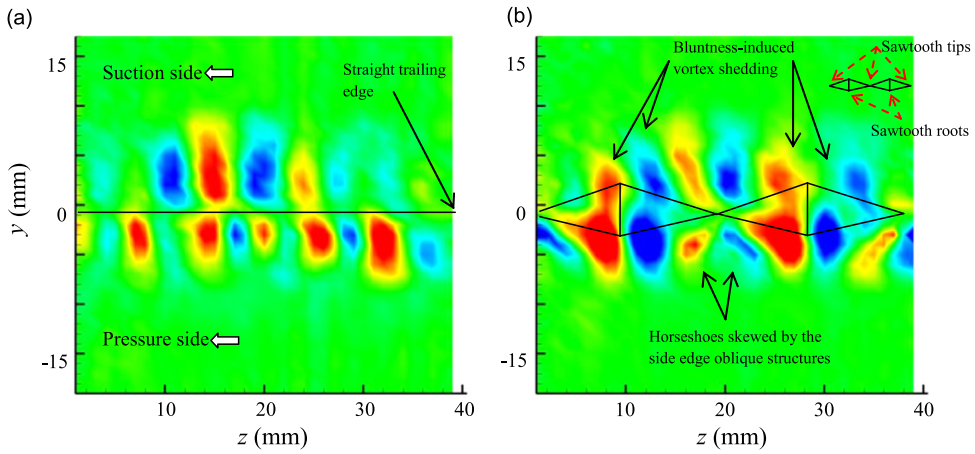

Fig. 26. Contours of streamwise vorticity produced by a NACA0012 airfoil at $x/C=1.03$, and 3° angle of attack, with a (a) straight trailing edge and (b) serrated sawtooth trailing edge of $2h=20$ mm and $\varphi=25°$.

observed for the serrated trailing edge. The *PSD* of u' and v' also reveal a prominent spectral hump, which suggests the presence of a strong vortex shedding near the sawtooth tip.

Cross spectral density analysis was performed near the sawtooth tip for the product of the boundary layer velocity fluctuations ($u'v'$) and the wall pressure fluctuation p' directly below the X-wire. A large level of cross spectral density near the sawtooth tip is noticed, which implies that the wall pressure fluctuation is mainly caused by the local boundary layer hydrodynamics. The cross spectral density results thus further exclude the effect of acoustical back scattering. Boundary layer velocity and wall pressure signals were also analyzed using the conditional-averaging technique to investigate the temporal variations of the coherent structures in the straight and serrated sawtooth trailing edges. Both the momentum and turbulence properties at the main body of the serrated sawtooth trailing edge are similar in characters to the straight trailing edge. Near the sawtooth oblique side edge, the turbulence substructures exhibit simultaneously weakened sweeping and ejection motions. Despite the shifting dynamics of the local turbulence transport, the mean turbulence level remains about the same across the boundary layer. However, near the sawtooth tip, an extensive flow mixing between the turbulent boundary layer and the pressure-driven vortical structure is clearly demonstrated.

The identification of the pressure-driven, oblique vortical structures and their interaction with the nominally turbulent boundary layer warrants further investigation. The analysis now focuses on the convection velocity of the turbulent eddies on the straight and serrated sawtooth trailing edges. Assuming that Taylor's hypothesis is true for the propagating turbulent eddies, the phase spectrum between a pair of microphone sensors can be used to calculate the convection velocities U_c (Eq. (2)). The results of seven configurations are summarized in Table 1. Note that, as far as the straight trailing edge is concerned, a larger convection velocity is generally observed for the cases when the microphone sensors are spaced obliquely (i.e. Δx and $\Delta z>0$) compared with the case when only streamwise separation is present. This is because for an oblique separation the gradient $d\phi(f)/df$ from the phase spectrum becomes smaller, and the slightly increased effective distance $\Delta l=(\Delta x^2+\Delta z^2)^{0.5}$.

The differences in convection velocity between the straight and serrated sawtooth trailing edges (ΔU_c) remain small when the microphone sensors are separated by $\Delta x=4$ mm and $\Delta z=0$ (i.e. the B4–C3 and B2–C1 cases in Table 1). Conversely, as shown in Table 1, large differences in ΔU_c have been observed between the straight and serrated trailing edges for the cases B1–C1 (47% difference), C1–D1 (58% difference) and D1–E1 (44% difference). These microphone pairs share the same characteristics of $\Delta x=4$ mm and $\Delta z=2$ mm. Most importantly, they are all located very near the sawtooth side edge. However, the difference in convection velocities along the serration angle becomes small again further away from the sawtooth side edge, e.g. B2–C2 and C2–D2 in Table 1.

According to Amiet [12] and Howe [24], the wetted spanwise extent of the trailing edge is proportional to the radiated noise level. Despite the minor variation of I_y, as well as the increase of S_{qq} for a serrated sawtooth trailing edge discussed earlier, it is interesting that noise reduction can still be achieved despite the fact that the ratio of the wetted lengths between a straight trailing edge and a serrated sawtooth trailing edge is equal to $sin(\varphi)$. The reasons might be related to Howe's theory [6], which is also summarized in Gruber et al. [9]. They stated that not all the boundary layer turbulence wavenumber components could scatter efficiently into noise by a serrated sawtooth trailing edge, except those that arrive near perpendicularly to the serration angle φ. However, wavenumber components that deviate from the mean flow direction can also affect the radiation integral term and subsequently the noise scattering. Therefore, the serration is acting as a filter for the turbulence wavenumber components.

Howe's theory could be further supplemented by the presence of vortical structures along the sawtooth side edges. Fig. 25 represents several schematics showing the propagations of boundary layer pressure waves at different trailing edges. Because the wall pressure S_{qq} is generally dominated by the streamwise wavenumber components in the convective region,

consideration is only given to the boundary layer pressure wave that propagates at a small angle, φ', with respect to the mean flow direction. Case A and Case C represent $+\varphi'$ and $-\varphi'$ respectively, while Case B represents $\varphi'=0^\circ$. For all cases, noise should be scattered at both the tip and side edges of the sawtooth. The mechanisms proposed by Howe [6] and Gruber et al. [9] on the noise reduction by a serrated sawtooth trailing edge are likely to be suitable for Case B and Case C. In Case A, the boundary layer pressure waves will propagate in an angle close to the oblique vortical structures. The interaction between them has been shown to cause a significant reduction of momentum of the boundary layer pressure waves. The kinetic energy of the disturbances, which is about the square of the convective velocity, will also be reduced. Ultimately, noise scattering will be less effective for this particular case.

According to Howe [6], a sawtooth trailing edge can potentially achieve self noise reduction up to $10\times\log_{10}\left(1+(1/\tan\varphi)^2\right)$ dB. Although it remains debatable if such an asymptotic level can be realistically achieved, it has been universally agreed that a maximum noise reduction would require the serration angle φ to be small. This specification is associated with the angle between the sawtooth side edge and the boundary layer pressure waves, $(\varphi-\varphi')$. If $(\varphi-\varphi')\rightarrow 0$, or $\varphi'\approx\varphi$, the level of momentum reduction of the boundary layer pressure waves in Case A is expected to be the greatest because they are propagating almost parallel with the sawtooth side edges/vortical structures. Based on the results in Table 1, the momentum loss of the boundary layer substructure could be as high as 50%. On the other hand, the most effective noise scattering should occur at a small value of φ'. The above two conditions stipulate that a narrow serration will be more effective in noise reduction.

Another explanation is that the vortical structure will also occupy more surface area per sawtooth for a narrow-angle than a wide-angle serrated sawtooth. This is supported by comparison of the liquid crystal results between a wide-angle sawtooth and a narrow-angle sawtooth (Fig. 5 versus Fig. 6), where both cases have the same $2h$. Therefore, noise scattering at the tips and side edges of the narrow-angle sawtooth will be weaker, despite the fact that the total length of the wetted serrated edge per unit span, and the total number of sawtooth tips, are actually increased.

8. Outlook

All the results presented thus far are related to the turbulent flow over one side of a flat plate where there is no flow on the other side. The question remains whether the flow physics pertinent to the present study can also be applied to the airfoil case where flow exists on both the suction and pressure surfaces. Although it is beyond the scope of the current paper to thoroughly investigate this issue, we have performed an experiment to study the wake field produced by a NACA0012 airfoil with a straight trailing edge and a serrated trailing edge.

The NACA0012 airfoil is the same one already used in our previous study [10]. Boundary layer tripping elements were applied close to the leading edges of both the suction and pressure sides. The serrated trailing edge of the airfoil (S3), which has exactly the same sawtooth geometrical parameters as the current flat plate case, can achieve up to 5 dB broadband noise sound power reduction [10]. The rationale behind the airfoil wake experiment is to examine whether the footprints of the oblique vortical structure can be found in the airfoil's near wake.

Fig. 26a shows the streamwise vorticity contour in y–z plane at $x/C=1.03$ for the airfoil with a straight trailing edge. C is the airfoil chord. The freestream velocity is 30 m s^{-1} and the airfoil is set at 3° angle of attack. The streamwise vorticity produced by the serrated trailing edge is plotted in Fig. 26b. Note that due to the nonflat plate type serration [10], certain degree of bluntness (5.7 mm) is exposed at each of the sawtooth roots.

For the straight trailing edge, the wake flow is characterized by alternately positive and negative regions of streamwise vorticity across the span of the airfoil. This is common in a wake flow where spanwise rib-like structures are present. However, for the serrated trailing edge, the wake field is more complex. At the region close to the sawtooth roots, large streamwise vortical structures are developed across the suction and pressure sides, which is caused by the bluntness-induced vortex shedding emanated from the sawtooth roots. At the region of the sawtooth tips, the otherwise rib-like structures become more skewed and oblique in shape (especially at the pressure side) and they also tend to mirror around the sawtooth tip. This suggests that the wake structure could be influenced by the side edge oblique structures originated from the sawtooth surface. The results in Fig. 26 thus provide a hint that the side edge oblique vortical structure observed in the flat plate configuration might also be present in the airfoil case. More details about such interaction and its implication to the radiated noise remain to be investigated.

9. Conclusion

Noise measurements in an anechoic chamber confirm that turbulent broadband noise reduction can be achieved by a serrated sawtooth trailing edge in a flat plate configuration. The investigation then focuses on the velocity and thermal properties of turbulent boundary layer on a serrated sawtooth surface in order to establish the causal relationship between the noise and the near field observations. Noise reduction is found to occur at a fairly large frequency range. The same frequency range is also associated with high levels of wall pressure power spectral density near the sawtooth tip and the sawtooth side edges. Initially, the dominant fluctuating components occupy mainly at region close to the sawtooth tip. At higher frequency, these structures will shift to the sawtooth side edges and slowly disappearing altogether outside the frequency range where noise reduction ceases to exist.

Both the turbulent boundary layers on a straight trailing edge, and on a serrated sawtooth trailing edge, contain coherent structures in the form of hairpin-type vortices to regenerate themselves through the sweep-and-eject mechanism. However, by conditional-averaging the turbulent boundary layer, the results suggest that the properties of the hairpin vortices on a serrated sawtooth trailing edge cannot be the only driving force for the noise reduction. It was found that the interaction between the hairpin vortices and the non-viscous, pressure-driven oblique vortices is the main reason to produce the significant levels of heat transfer/wall pressure fluctuation (S_{qq}) as well as the reduction in convection rate of the turbulence structures near the sawtooth tip and the side edges.

Based on the Amiet's model, the increase of S_{qq} near the sawtooth side edges and sawtooth tip should have increased the radiated noise level S_{pp}. We conjecture that this effect, however, is small in comparison with the significant loss in momentum of the boundary layer substructure near the sawtooth side edges through the viscid–inviscid interaction between the turbulent eddies and the oblique vortical structures, respectively. This interaction provides an effective mechanism for the redistribution of the momentum and turbulent shear stress near the sawtooth tip and side edges, and reduces the scattering-efficiency of the hydrodynamic pressure waves into trailing edge noise.

Acknowledgment

The authors are grateful for the support from the EPSRC Doctoral Training Grants in the United Kingdom.

References

[1] A. Wolf, T.H. Lutz, W. Wurz, E. Kramer, O. Stalnov, A. Seifert, Trailing edge noise reduction of wind turbine blades by active flow control, *Wind Energy* 18 (2015) 909.
[2] A. Inasawa, C. Ninomiya, M. Asai, Suppression of tonal trailing-edge noise from an airfoil using a plasma actuator, *AIAA Journal* 51 (2013) 1695.
[3] O. Rodriguez, Base drag reduction by control of the three-dimensional unsteady vortical structure, *Experiments in Fluids* 11 (1991) 218.
[4] A.M. Knepper, Examination of Three Candidate Technologies for High-lift Devices on Aircraft Wing, PhD thesis, Cranfield University, 2005.
[5] M.S. Howe, Aerodynamic noise of a serrated trailing edge, *Journal of Fluids and Structure* 5 (1990) 33.
[6] M.S. Howe, Noise produced by a sawtooth trailing edge, *Journal of the Acoustical Society of America* 90 (1991) 482.
[7] K. Braun, N. Van der Borg, A. Dassen, F. Doorenspleet, A. Gordner, J. Ocker, R. Parchen, Serrated trailing edge noise (STENO), *Proceedings of the European Wind Energy Conference*, Nice, France, James & James (Science Publishers) Ltd., London, UK, 1999, p. 180.
[8] S. Oerlemans, M. Fisher, T. Maeder, K. Kögler, Reduction of wind turbine noise using optimized airfoils and trailing-edge serrations, *AIAA Journal* 47 (2009) 1470.
[9] M. Gruber, P.F. Joseph, T.P. Chong, On the mechanisms of serrated airfoil trailing edge noise reduction, AIAA Paper No. 2011-2781, 2011.
[10] T.P. Chong, A. Vathylakis, P.F. Joseph, M. Gruber, Self-noise produced by an airfoil with nonflat plate trailing-edge serrations, *AIAA Journal* 51 (2013) 2665.
[11] J. Hurault, A. Gupta, E. Sloth, N.C. Nielsen, A. Borgoltz, P. Ravetta, Aeroacoustic wind tunnel experiment for serration design optimisation and its application to a wind turbine rotor, Proceedings of the 6th International Meeting on Wind Turbine Noise, Glasgow 2015.
[12] R. Amiet, Noise due to turbulent flow past a trailing edge, *Journal of Sound and Vibration* 47 (1976) 387.
[13] D.M. Chase, The character of the turbulent wall pressure spectrum at subconvective wavenumbers and a suggested comprehensive model, *Journal of Sound and Vibration* 112 (1987) 125.
[14] T.P. Chong, P.F. Joseph, An experimental study of airfoil instability tonal noise with trailing edge serrations, *Journal of Sound and Vibration* 332 (2013) 6335.
[15] D.J. Moreau, C.J. Doolan, Noise-reduction mechanism of a flat-plate serrated trailing edge, *AIAA Journal* 51 (2013) 2513.
[16] S. Pröbsting, Coherent Structures at the Serrated Trailing-edge of a NACA 0012, Master of Science thesis, Delft University of Technology, 2011.
[17] A. Vathylakis, J.H. Kim, T.P. Chong, Design of a low-noise aeroacoustic wind tunnel facility at Brunel University, AIAA Paper No. 2014-3288, 2014.
[18] P.T. Ireland, Z. Wang, T.V. Jones, Liquid crystal heat transfer measurements, *Von Karman Institute for Fluid Dynamics 1992–1993 Lecture Series*, 1993.
[19] J.W. Baughn, Liquid crystal methods for studying turbulent heat transfer, *International Journal of Heat and Fluid Flow* 16 (1995) 365.
[20] S. Zhong, T.P. Chong, H.P. Hodson, A comparison of spreading angles of turbulent wedges in velocity and thermal boundary layers, *Journal of Fluids Engineering – Transactions of ASME* 125 (2003) 267.
[21] A. Vathylakis, T.P. Chong, On the turbulent boundary layers developed on flat plate with a serrated trailing edge, AIAA Paper No. 2013-2107, 2013.
[22] L.W.B. Browne, R.A. Antonia, L.P. Chua, Calibration of X-probes for turbulent flow measurements, *Experiments in Fluids* 7 (1989) 201.
[23] I.C. Lekakis, R.J. Adrian, B.G. Jones, Measurement of velocity vectors with orthogonal and non-orthogonal triple-sensor probes, *Experiments in Fluids* 7 (1989) 228.
[24] M.S. Howe, A review of the theory of trailing edge noise, *Journal of Sound and Vibration* 61 (1978) 437.
[25] T.F. Brooks, T.H. Hodgson, Trailing edge noise prediction from measured surface pressures, *Journal of Sound and Vibration* 78 (1981) 69.
[26] A.G. Sagrado, Boundary Layer and Trailing Edge Noise Sources, PhD thesis, University of Cambridge, 2007.
[27] M.I. Daoud, Stochastic Estimation of the Flow Structure Downstream of a Separating/Reattaching Flow Region Using Wall–Pressure Array Measurements, PhD thesis, Michigan State University, 2004.
[28] W.C. Reynolds, A.K.M.F. Hussain, The mechanics of an organized wave in turbulent shear flow. Part 3. Theoretical models and comparisons with experiments, *Journal of Fluid Mechanics* 54 (1972) 263.
[29] B. Cantwell, D. Coles, An experimental study of entrainment and transport in the turbulent near wake of a circular cylinder, *Journal of Fluid Mechanics* 136 (1983) 321.
[30] R.J. Adrian, P. Moin, R.D. Moser, Stochastic estimation of conditional eddies in channel flow, Report CTR-S87, Center for Turbulence Research, NASA Ames/Stanford, 1987.
[31] Y.G. Guezennec, Stochastic estimation of coherent structures in turbulent boundary layers, *Physics of Fluids* A1 (1989) 1054.
[32] H.T. Kim, S.J. Kline, W.C. Reynolds, The production of turbulence near a smooth wall in a turbulent boundary layer, *Journal of Fluid Mechanics* 50 (1971) 133.
[33] M.R. Head, P. Bandyopadhyay, New aspects of turbulent boundary-layer structure, *Journal of Fluid Mechanics* 107 (1981) 297.
[34] R.L. Panton, Overview of the self-sustaining mechanisms of wall turbulence, *Progress in Aerospace Sciences* 37 (2001) 341.